Journal of Materials Processing Tech. 348 (2026) 119197

Contents lists available at ScienceDirect

Journal of Materials Processing Tech.

journal homepage: www.elsevier.com/locate/jmatprotec

Research article

Role of laser beam shape and energy density in modulating surface quality, porosity, microstructure, and mechanical properties of PBF-LB/M Ti-6Al-4V

Abid Ullah [a,b,*], Alexander E. Medvedev [a], Dirk Herzog [b,c], Andrey Molotnikov [a], Tingting Liu [d], Ingomar Kelbassa [b,c], Milan Brandt [a,**]

[a] RMIT Centre for Additive Manufacturing, RMIT University, Melbourne, VIC 3000, Australia
[b] Institute for Industrialization of Smart Materials, Hamburg University of Technology, Hamburg D-21079, Germany
[c] Fraunhofer IAPT, Hamburg D-20129, Germany
[d] School of Mechanical Engineering, Nanjing University of Science and Technology, Nanjing 210094, China

ARTICLE INFO

Keywords:
Additive Manufacturing
PBF-LB/M
Beam Shaping
Surface Quality
Porosity
Microstructure
Texture
Mechanical Properties
Ti-6Al-4V

ABSTRACT

Beam shaping has recently gained attention as a means to mitigate the thermal gradients and melt-pool instabilities associated with conventional Gaussian beams in laser powder bed fusion (PBF-LB/M), which often lead to surface roughness, defects, and microstructural inconsistency. This study examines the effects of different beam shapes and volumetric energy densities (VEDs) on the surface quality, porosity, microstructure, and mechanical response of Ti-6Al-4V. Cubic specimens were fabricated on an Aconity MIDI+ system using Gaussian, core-ring, and ring beam profiles over a VED range of 78–341 J/mm^3 . The results show that beam shaping with optimized VED reduces porosity, refines microstructure, and enhances mechanical performance. The Gaussian beam performed well at low VEDs (≤130 J/mm^3) but exhibited increased surface roughness and keyhole porosity at higher energy inputs (≥150 J/mm^3), whereas the ring-based beams initially showed higher porosity at low VEDs but achieved ∼99.97 % relative density and smoother surfaces at higher VEDs. The ring beam promoted stable conduction-mode melting, continuous prior-β grain growth, refined α′ martensitic microstructures, and strong crystallographic texture. From a mechanical perspective, Vickers hardness values (370–400 HV) correlated with the observed microstructural features. In addition, the Gaussian beam exhibited higher indicative strength at low VEDs but deteriorated with increasing energy input, whereas the ring beam showed the opposite trend, reaching an ultimate tensile strength of 1192 MPa and ∼21 % ductility under optimal conditions. Beam behavior was further evaluated using areal energy density (AED) normalized to the melt-pool width, indicating that melt-pool stability and the resulting surface quality, porosity, and microstructural evolution are primarily influenced by the spatial distribution of laser energy rather than nominal energy metrics alone. These findings provide a physical basis for laser beam shaping as an effective approach to broaden the stable processing window and achieve defect-free, texture-controlled Ti-6Al-4V components.

1. Introduction

Despite the rapid adoption and growth of metal laser powder bed fusion (PBF-LB/M) in industrial applications, the process continues to face challenges in simultaneously achieving stable quality, reliability, and productivity [1,2]. These challenges largely arise from the complex and dynamic nature of the laser–material interaction, which governs melt-pool behavior and consequent defect formation. In PBF-LB/M, the characteristics of the laser beam critically influence the resulting microstructure and properties. Specifically, the laser beam's shape, which refers to the controlled redistribution of energy across its cross-section, plays a critical role in influencing key aspects of the process, including melt pool geometry, thermal gradients, and solidification behavior of the material [3,4]. While such effects have been recognized in laser welding [5,6], their systematic quantification and transfer to PBF-LB/M remain limited, particularly under the complex multi-track, multi-layer conditions typical of additive manufacturing (AM) [7,8]. Conventionally, PBF-LB/M systems employ a Gaussian beam shape,

---

* Corresponding author at: RMIT Centre for Additive Manufacturing, RMIT University, Melbourne, VIC 3000, Australia.
** Corresponding author.
E-mail addresses: abid.ullah@tuhh.de, abidmech95@gmail.com (A. Ullah), milan.brandt@rmit.edu.au (M. Brandt).

https://doi.org/10.1016/j.jmatprotec.2026.119197
Received 8 September 2025; Received in revised form 31 December 2025; Accepted 1 January 2026

named for its intensity profile, which follows a Gaussian distribution. This profile is typical of certain laser types, such as fiber lasers, which are widely used in PBF-LB/M due to their reliable availability and high beam quality ($M^2 \approx 1$, meaning near-ideal beam focusability). Gaussian beams are known for their excellent beam characteristics, minimal divergence, and high spatial coherence, properties that make them well-suited for precise laser applications [8]. However, with growing demands for productivity and quality, the intrinsic instability of Gaussian beam-based melting has become a fundamental bottleneck in PBF-LB/M.

Gaussian beams are defined by strong intensity localization within the $1/e^2$ beam waist, containing 86 % of the incident power [9,10]. This concentrated central peak creates steep thermal gradients and localized overheating, and inadequate control of thermal distribution complicates laser–material interaction and the stability of the molten region, often resulting in various process-induced defects. Emerging research underscores that the Gaussian intensity profile, widely used in laser welding and PBF-LB/M, can intensify localized overheating, triggering evaporation, spattering, and dynamic instabilities within the liquid metal [11,12], as well as defects such as keyhole porosity [13,14] and frequent balling [15,16]. These consequences of unstable melt pool dynamics negatively affect the continuity of the melt track, stability, and part quality, thereby restricting the available processing window. The pronounced peak intensity leads to sharp thermal gradients and rapid solidification, which further limits the ability to produce defect-free parts [17,18]. Consequently, the shape of the laser beam plays a crucial role in determining the morphology of the molten zone, process consistency, productivity, surface quality, and the resulting microstructure. Expanding the beam with a zoom lens does not overcome these issues, as the resulting profile remains Gaussian and susceptible to the same drawbacks. Similarly, working off-focus to enlarge the beam still retains the suboptimal Gaussian profile and narrows the process window due to rapid variations in beam size along the propagation direction [7,19]. To overcome these challenges, alternative non-Gaussian beam profiles have been developed to achieve a more uniform heat distribution and improve process stability in PBF-LB/M. Originally derived from laser welding applications [20,21], beam profiles, such as ring-core, ring-shaped, and elliptical beams, redistribute energy away from the center. This reduces peak intensity and thermal gradients and promotes more stable melt-pool behavior. While initial investigations have demonstrated notable improvements, the implementation of laser beam shaping in PBF-LB/M remains in its early stages and warrants further research. Productivity suffers from a Gaussian beam because its concentrated peak intensity restricts the usable process window, forcing lower energy input to avoid defects, which directly limits build rate and overall productivity [22,23]. Although several studies have reported reduced spatter formation, improved build rates, and wider process windows [24,25], most have concentrated on qualitative process monitoring, with limited quantitative assessment of porosity, surface morphology, and detailed microstructural or phase evolution.

Ti-6Al-4V is among the most widely used alloys in AM, especially for aerospace and biomedical applications, due to its high strength-to-weight ratio and excellent corrosion resistance. The inherent limitations of the Gaussian profile are highly relevant for Ti-6Al-4V, as they constrain the achievable build rates and part quality that are critical for this material's demanding applications. In PBF-LB/M processing, Ti-6Al-4V is highly susceptible to process-induced defects such as porosity and surface roughness, which are strongly linked to the melt pool instabilities associated with conventional Gaussian profile [26,27], directly compromising the mechanical performance of the final parts [28,29]. However, as with other materials, comprehensive analyses linking beam shape to surface quality, internal porosity, and phase or texture development in bulk builds remain limited. Beam shaping offers a promising approach to mitigate these challenges and enhance process robustness for Ti-6Al-4V components, as initially explored in the previous single-track study [30]. Therefore, this study aims to fill these gaps by systematically investigating how different beam shapes, combined with controlled energy inputs, influence the surface morphology, porosity, microstructure, and mechanical properties of PBF-LB/M Ti-6Al-4V. By normalizing the energy input using areal energy density (AED) and directly correlating beam profile to process and material outcomes, this work provides a mechanistic understanding of how laser spatial energy distribution governs melt-pool stability and part quality, thereby defining a physical framework for expanding the stable processing window in Ti-6Al-4V.

2. Methods

2.1. Materials and processing

The experiments in this work were conducted using gas-atomized Ti-6Al-4V Grade 5 powder supplied by ECKART TLS GmbH (Bitterfeld, Germany). The powder exhibited spherical morphology with a characteristic particle size distribution of D10 = 26.72 μm, D50 = 37.93 μm, and D90 = 50.18 μm, and a nominal size range of 15–45 μm as specified by the manufacturer. The chemical composition of the powder provided by the supplier is listed in Table 1. All specimens were fabricated using a PBF-LB/M system (Aconity MIDI+, Aconity3D GmbH, Germany), operated through the web-based control software AconitySTUDIO. The system is equipped with an nLIGHT AFX multi-mode fiber laser capable of delivering up to 1200 W of power. The optical setup includes an F-theta lens providing a standard spot size of 130 μm, which can be adjusted up to 500 μm for three-dimensional scanning applications. The AFX laser allows modulation of the beam profile from a Gaussian (Mode 0) to a ring-shaped (Mode 6), with five intermediate modes that progressively redistribute more power toward the beam edge, thereby increasing the minimum spot size. In this study, three distinct beam profiles were used to manufacture 10 × 10 × 10 mm^3 Ti-6Al-4V specimens: Mode 0 (edge-to-core ratio = 00:100), Mode 3 (54:46), and Mode 6 (89:11), as illustrated in Fig. 1.

The process parameters used in this study were developed as an extension of the previously reported single-track investigation [30], while additional adjustments were made to suit the specific objectives and conditions of the present work. Laser power was varied from 150 W to 250 W and scanning speed from 250 mm/s to 650 mm/s for each beam profile, while keeping other parameters constant, including a layer thickness of 30 μm and a hatch spacing of 98 μm. A relatively low layer thickness was selected to ensure better melt pool stability and interlayer bonding while minimizing the risk of lack-of-fusion defects across all beam profiles and energy inputs. To maintain consistent processing conditions, a bidirectional hatch scanning strategy with 90° interlayer rotation was used for all beam profiles. The volumetric energy density (VED) was calculated using Eq. 1, producing values between 78.49 J/mm^3 and 342.47 J/mm^3 .

$$VED = \frac{P}{v \cdot h \cdot t} \quad \left[\frac{J}{mm^3}\right] \tag{1}$$

where P is the laser power (W), v is the scan speed (mm/s), h is the hatch spacing (mm), and t is the layer thickness. The selected VED range covers both lack-of-fusion and keyhole regimes and was established through several single-track trials to provide the most reliable basis for comparing the influence of different beam shapes. To account for beam-size effects, the effective interaction width measured from corresponding single-track experiments conducted under the same processing conditions in the previous study [30] was used to calculate the areal

Table 1
Chemical composition of Ti-6Al-4V virgin powder feedstock (wt%).

Element	N	C	H	Fe	O	Al	V	Ti
Measured	0.008	0.003	0.002	0.20	0.11	6.29	3.98	Bal.

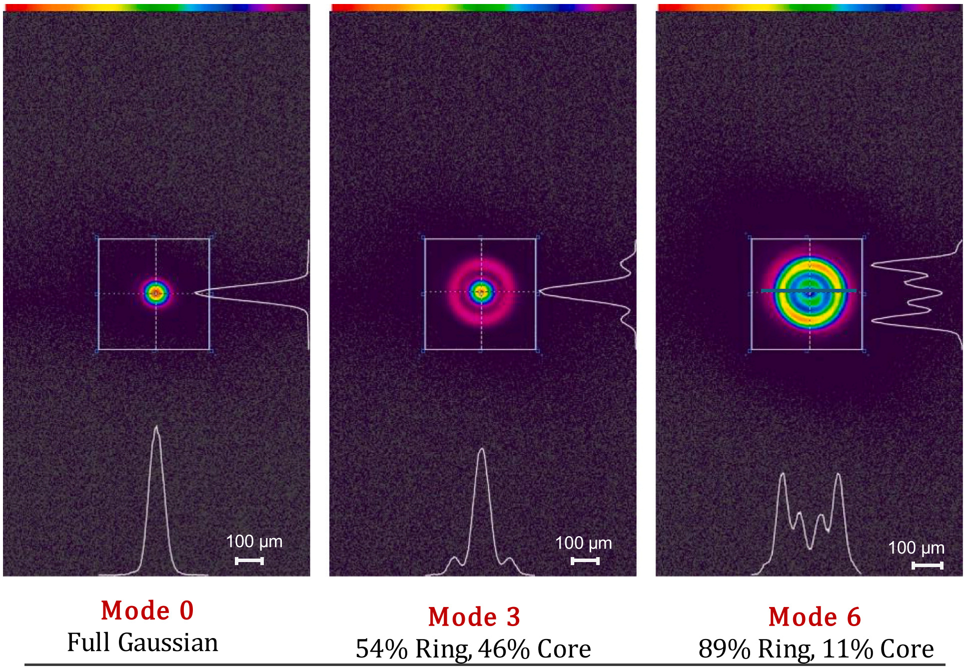

Mode 0
Full Gaussian

Mode 3
54% Ring, 46% Core

Mode 6
89% Ring, 11% Core

Fig. 1. Near-field beam profiles of the laser modes used in this study: Gaussian (Mode 0), Mixed Ring-Core (Mode 3), and Ring (Mode 6), illustrating the transition from a fully Gaussian to a predominantly ring-shaped intensity distribution (courtesy of Aconity GmbH).

energy density ($\mathrm{AED}_{\mathrm{track}}$).

$$\mathrm{AED}_{\mathrm{track}} = \frac{P}{v w_{\mathrm{track}}} \quad \left[\frac{J}{\mathrm{mm}^2}\right] \tag{2}$$

where P is the laser power (W), v is the scan speed (mm/s), and w is the measured melt-pool width (mm). The calculated $\mathrm{AED}_{\mathrm{track}}$ ranged approximately from 1.0 to 2.8 J/mm^2 across all beam profiles. This metric reflects the practical influence of the beam's effective spot size on the melt-pool behavior. Table 2 summarizes the combinations of beam profiles and parameters used for specimen fabrication.

2.2. Surface and microstructural characterization

Non-destructive volumetric characterization was first conducted using micro-CT scanning with a Diondo Evo05 system (Diondo GmbH, Germany) to detect and quantify internal defects such as pores, inclusions, and lack-of-fusion voids. Scans were performed at 150 kV and 66 µA with an integration time of 190 ms, achieving a voxel resolution of 15 µm. The reconstructed 3D volume data from a total of 27 cube samples were analyzed using VGSTUDIO MAX (Volume Graphics GmbH, Germany). Porosity analysis followed the standard procedure described by du Plessis et al. [31]. Relative density was calculated from the total pore volume segmented from each micro-CT–scanned cube and cross-validated with optical microscopy measurements on polished cross-sections, the averaged values are reported. In cases where direct volume data were missing or inconsistent, pore volume was estimated using the equivalent diameter and sphericity to ensure continuity across the dataset. Following micro-CT analysis, the as-built top and side-skin surface topographies of the cube samples were examined using a Keyence 3D Laser Scanning Confocal Microscope (VK-X160K, Keyence Corporation, Osaka, Japan) for high-resolution, non-contact 3D measurements. In this study, the top surface refers to the plane perpendicular to the build direction, while the side skin corresponds to the vertical planes parallel to the build direction. For each sample, an area of approximately 2000 × 1500 µm^2 was scanned with a vertical resolution (z-axis) of 1 µm. The surface roughness parameters evaluated were Sa and Sz. Sa represents the mean height of the surface area, calculated as the average of absolute deviations from the mean plane, whereas Sz is defined as the sum of the maximum peak height and maximum valley depth within the scanned area. The single-track specimens, provided for reference in this study, were produced using the same approach and characterization methods as reported in the previous single-track investigation [30].

For microstructural analysis, samples were subsequently mounted using a Buehler SimpliMet Metallurgical Mounting Press (Spectrographic Ltd, Hebden Bridge, UK), ground with silicon carbide sandpapers (P320–P4000), and polished sequentially with 9 µm, 3 µm, and 1 µm diamond suspensions on a Struers Rotopol-31 system. Final polishing was carried out on a VibroMet 2 vibration polisher for up to eight hours using MasterMet-2 colloidal silica suspension to achieve a deformation-free surface. To reveal surface features and microstructural details, the samples were etched with Kroll's solution (5 vol% HNO_3 and 2 vol% HF) for 10–12 s, neutralized with $CaCl_2$, and cleaned in an ultrasonic acetone bath. Detailed microstructural and surface analyses were then performed using a Zeiss Supra 55 VP Field Emission Scanning Electron Microscope (FEG-SEM, Carl Zeiss AG, Oberkochen, Germany). Electron backscatter diffraction (EBSD) analysis was performed on a JEOL 7200 F Schottky field emission SEM operated at 20 kV and equipped with an Oxford Instruments NordlysMax2 EBSD detector, using a step size of 0.20 µm. Data acquisition and post-processing were carried out using AZtec and AztecCrystal software to evaluate texture, phase distribution, β-phase reconstruction, and misorientation.

Table 2
Laser processing parameters for each beam profile index.

Beam Profile	Nominal Spot diameter Ø (µm)	Laser power (W)	Scan speed (v)	VED Range (J/mm^3)
Mode 0	135	150, 200, 250	250, 450, 650	78–342
Mode 3	210	150, 200, 250	250, 450, 650	78–342
Mode 6	383	150, 200, 250	250, 450, 650	78–342

2.3. Mechanical characterization

2.3.1. Vickers microhardness testing

Vickers microhardness testing was performed using a DuraScan hardness tester (Struers) with a 0.1 kgf (HV0.1) load. Measurements were conducted on longitudinally cross-sectioned cuboid specimens. For each sample, 25 equidistant indentations were arranged in a 5 × 5 square grid with a spacing of 1.5 mm, covering a 6 mm × 6 mm area centered within the 10 mm × 10 mm cross-sectional surface. This layout ensured representative sampling across the build direction.

2.3.2. Instrumented indentation testing

Instrumented indentation tests were performed using an i3D WLI system (Imprintec GmbH, Bochum, Germany) with a 60 kg maximum load. The system records load-displacement curves and applies inverse finite element method (FEM) analysis according to DIN SPEC 4864:2019–11 procedure. The material behavior is described by the Ludwik hardening law:

$$\sigma = \sigma_0 + K_L \varepsilon^{n_L}$$

where σ is the true stress, σ_0 the initial yield strength, K_L the strength coefficient, ε the true strain, and n_L the strain-hardening exponent. A von Mises yield criterion is applied. The optimization routine iteratively minimizes the squared residual between simulated and experimental indentation profiles,

$$\sum_{i=1}^{n} \left(f(x_i;\sigma_0,K_L,n_L) - y_i\right)^2 = \text{res}$$

where $f(x_i;\sigma_0,K_L,n_L)$ is the simulated indentation height, y_i the measured height, and n the number of data points. Friction between indenter and specimen was set to $\mu = 0.1$ as recommended in the standard.

Each measurement was processed using the integrated FEM module, which outputs raw surface profiles, residual error checks, pile-up maps, and fitted contact areas to determine local properties such as bulk hardness index (HI), estimated yield strength ($R_{p0.2}$), ultimate tensile strength (UTS), ductility (D), and complete indentation-derived stress–strain curves. The correlation with conventional tensile properties is based on a calibrated material dataset derived from as-built PBF-LB/M Ti-6Al-4V tensile tests obtained through prior reference experiments and partner collaborations, including Fraunhofer IAPT (Germany). This approach ensures that the indentation-derived values provide a statistically reliable relative comparison rather than a direct substitute for conventional tensile testing. A representative indentation grid and yield strength map obtained from the Imprintec system are shown in Fig. 2, illustrating the measurement layout, property distribution, and data evaluation workflow. The local yield strength map shows slight spatial variations, where the blue regions indicate areas of relatively lower strength, likely due to minor local microstructural or porosity variations within the tested region. Additionally, 3D surface profiles of the indents were acquired to verify penetration geometry and pile-up behavior. In total, 24 cube specimens were analyzed across the different beam shapes and VED conditions to ensure statistical robustness of the local mechanical property data. This methodology and its correlation framework are consistent with established approaches for instrumented indentation and inverse FEM analysis applied to PBF-LB/M Ti-6Al-4V and other alloys, as reported in recent studies [32,33].

3. Results and discussion

3.1. Surface roughness assessment

The influence of beam shaping on the side-skin surface roughness of as-built Ti-6Al-4V specimens (xz-plane) was evaluated using average roughness (Sa) and peak-to-valley height (Sz). Variations across different volumetric energy densities (VEDs) reveal distinct trends for each beam profile, highlighting the critical role of beam shape in modulating laser–powder interactions and surface morphology. For the Gaussian beam (Mode 0), both Sa and Sz increase progressively with rising VED, as illustrated in the topography maps and line plots in Figs. 3 (a) and 4, respectively. The surface maps reveal pronounced topographical features, including sharp peaks and deep valleys, which are quantitatively reflected by elevated Sa and Sz values. These features are particularly prominent for Mode 0 at higher VEDs. As illustrated in Fig. 3 (a3) and 4, surface roughness increases substantially under Mode 0 as energy input rises. This trend is primarily attributed to the concentrated energy distribution of the Gaussian beam, which causes localized overheating and melt pool instabilities, particularly near scan endpoints. These effects lead to the formation of elevated edges and surface irregularities, consistent with observations reported by Metelkova et al. [34]. At high energy densities, excessive energy input induces melt pool turbulence, spattering, and material ejection, which degrade surface quality. This process is intensified by the formation of keyholes, resulting from recoil pressure due to flash evaporation of the molten metal [35,36]. Conversely, at low energy densities, insufficient fusion contributes to surface defects such as balling and incomplete melting. These dual effects of low and high VEDs on surface roughness have been widely reported [37,38]. The combined evidence indicates that Mode 0 provides a relatively narrow processing window for applications where minimal surface roughness is critical, particularly at elevated energy levels. The trends observed in Sa and Sz for Mode 0 (Figs. 3 and 4) are consistent with prior investigations into roughness evolution in PBF-LB/M of Ti-6Al-4V using a Gaussian beam profile [39,40].

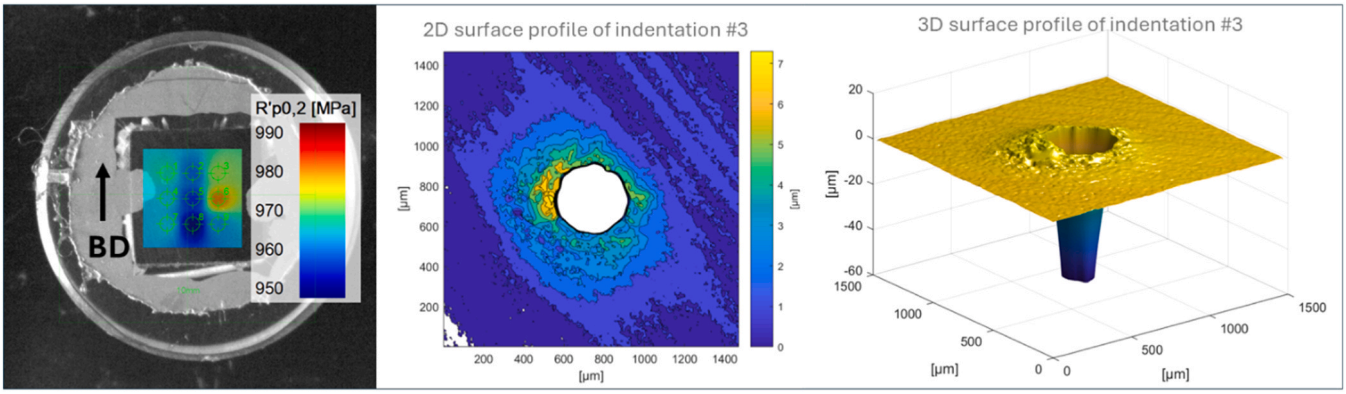

Fig. 2. A representative map of local yield strength ($R_{p0.2}$) acquired with the Imprintec system on the cross-section of a cube specimen (mounted in epoxy), showing its spatial distribution across a 9-point (3 × 3) indentation grid covering an area of approximately 5 × 5 mm (left). The 2D and 3D surface profiles of indentation No. 3 illustrate the actual penetration depth and surrounding pile-up, confirming the deformation volume used to derive the instrumented indentation stress–strain data.

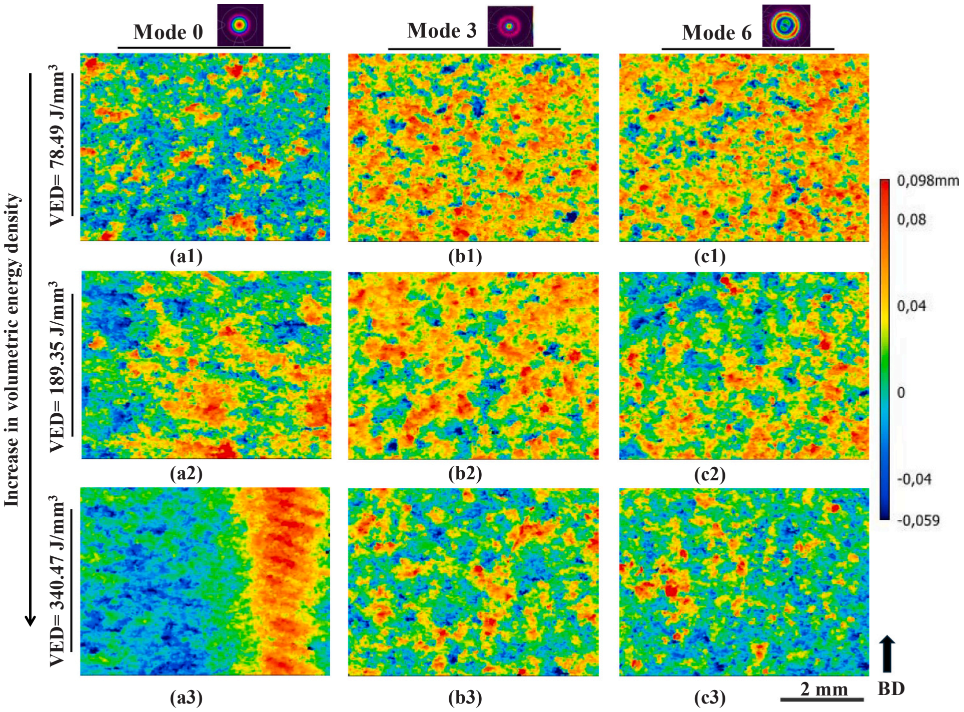

Fig. 3. As-built side-skin surface topography maps of Ti-6Al-4V cube specimens produced using Mode 0 (a1–a3), Mode 3 (b1–b3), and Mode 6 (c1–c3) at increasing VED levels (78.49–340.47 J/mm^3, top to bottom). The color scale indicates surface height, with red representing peaks and blue representing valleys. The build direction (BD) is indicated by the arrow.

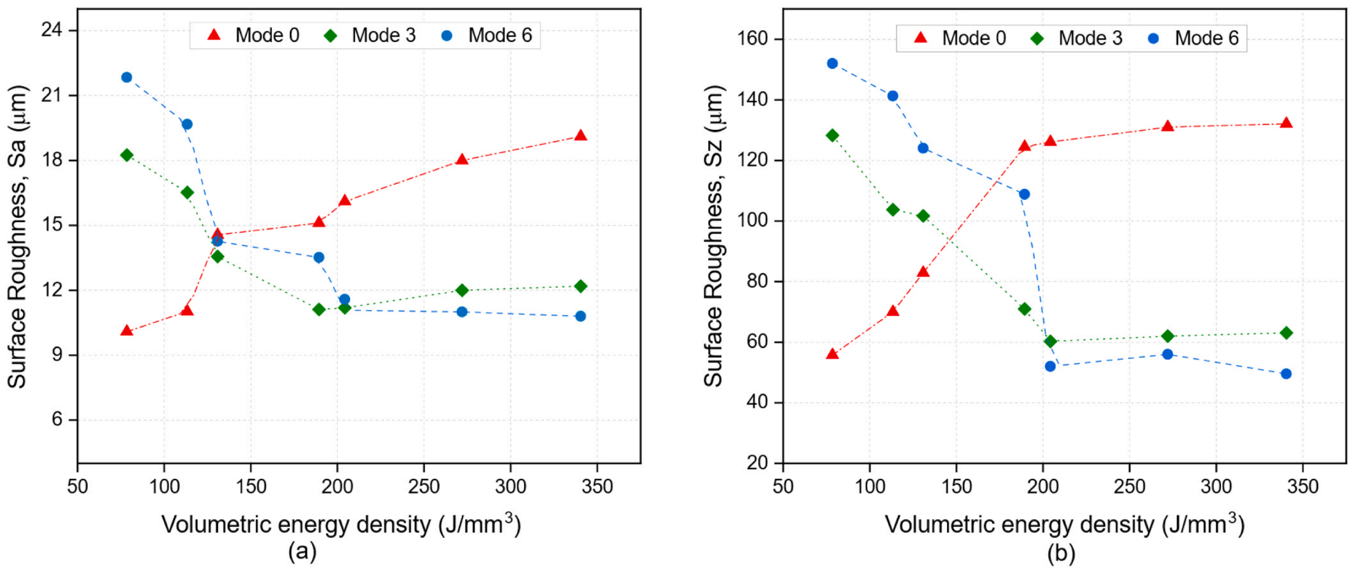

Fig. 4. (a) Surface roughness (*Sa*) and (b) peak-to-valley roughness (*Sz*) for Mode 0, Mode 3, and Mode 6 beam profiles across varying VED levels.

In contrast to Mode 0, both Mode 3 (ring-core) and Mode 6 (ring), which utilize ring-based energy distributions, exhibit higher surface roughness at lower VED levels (around 78.49 J/mm^3), likely due to insufficient melting and unstable melt pool conditions. However, as the VED increases, particularly beyond approximately 189 J/mm^3 , surface quality improves significantly, indicating enhanced melt pool stability and more consistent fusion. Among all beam profiles, Mode 6 consistently produces lower surface roughness at the high energy input (VED = 340.47 J/mm^3), as reflected by the reduced Sa and Sz values in Fig. 4. This improvement is also evident in the surface maps in Fig. 3 (c3), where Mode 6 displays fewer topographical fluctuations and a more uniform texture compared to the other beam profiles. The more consistent surface texture achieved with the ring-based beams indicates enhanced melt-pool stability, which originates from their ring-shaped energy distribution that redistributes energy laterally and broadens the melt-pool cross-section. This reduces temperature gradients and suppresses the onset of keyholing and spatter formation.

To further interpret these observations, it is essential to consider the underlying melt-pool fluid dynamics that govern surface morphology. Once keyhole formation begins, the steep thermal gradients in the Gaussian beam produce strong recoil pressure and drive outward Marangoni convection along the molten surface [41], which destabilizes the rim and amplifies surface irregularities. In contrast, the annular energy distribution of the ring-shaped beam redistributes laser power laterally, forming a shallower and wider melt pool with reduced pressure gradients and a more stable free surface. This lateral energy spread minimizes surface deformation and suppresses humping and excessive rippling phenomena. The underlying flow behavior can be further explained by the balance between Marangoni convection and recoil pressure. Under Gaussian heating, strong central input drives vigorous outward surface-tension-driven flow coupled with vapor recoil, and these oscillations associated with Plateau–Rayleigh and Kelvin–Helmholtz instabilities lead to wave-like solidification and rough surfaces [39]. The ring beam, on the other hand, weakens the center-outward velocity component and promotes symmetric convection within the melt pool, stabilizing the free surface. Consequently, the molten metal solidifies with reduced oscillatory motion, producing smoother and more uniform surfaces, as also reported by Bauch et al. [42].

This mechanism is further supported by the single-track observations, which demonstrate the transition from unstable to stable melt-pool behavior under different beam profiles. To illustrate the physical basis of surface roughness evolution, representative single-track morphologies obtained under comparable beam profiles and energy-input ranges are shown in Fig. 5 to visualize melt-pool stability transitions and surface-formation behaviors. The representative top-view, 3D topography, and cross-sectional images depict typical surface features, including ripples, spattering, necking, and track interruption (balling), that correspond to distinct melt-pool stability regimes. At relatively high energy inputs, the Gaussian beam induces keyhole formation and strong recoil-pressure oscillations, producing spattering and irregular solidification fronts, whereas the ring-based beams maintain a conduction-mode melt pool with smoother flow and solidification, resulting in uniform surface profiles. At lower VEDs, however, insufficient melting in the ring-based beams leads to track interruption and balling, which locally increases surface roughness, as observed in Fig. 3. In the study by Kohlwes et al. [43], high-speed imaging and numerical simulations confirmed that ring-shaped beams generated up to six times fewer spatters owing to their lower temperature gradients and reduced vapor recoil, which stabilized the free surface. Quantitative analysis of the single tracks revealed a ~25–30 % reduction in melt-pool height

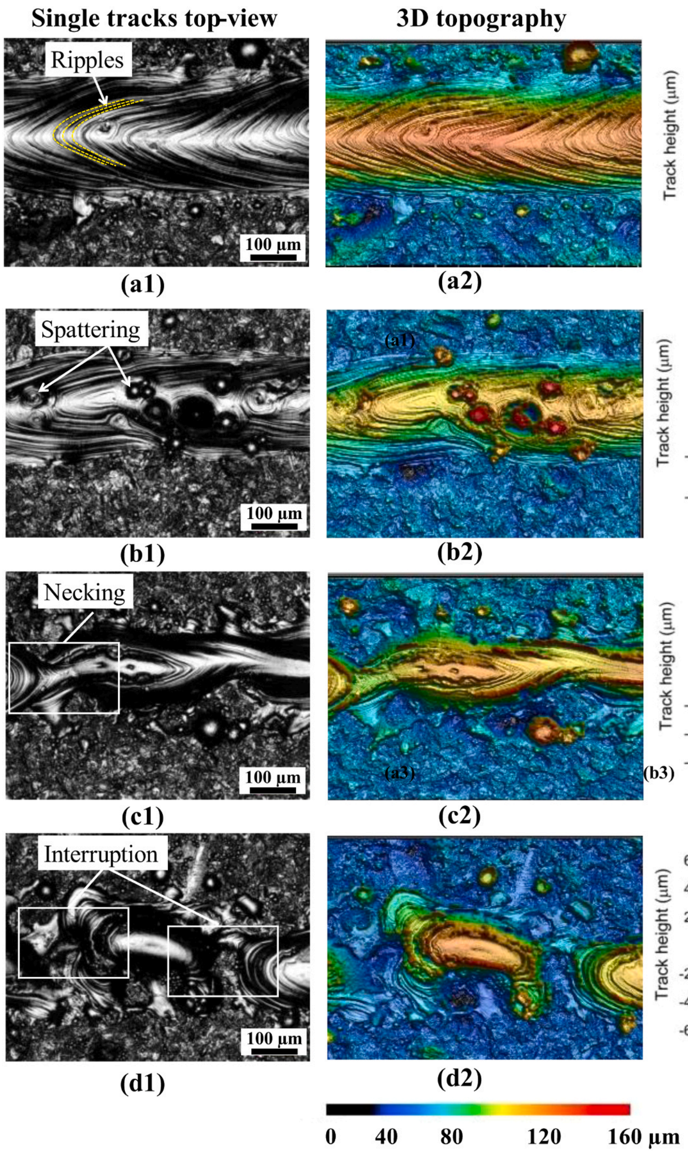

Fig. 5. Representative single-track morphologies illustrating surface-roughness formation mechanisms in PBF-LB/M Ti-6Al-4V. Each row presents the top-view, 3D surface topography, track-height profile, and melt-pool cross-section. (a1–a3) Ring beam at high energy: stable, continuous tracks with mild rippling due to surface-tension oscillations (b1–b3) Gaussian beam at high energy: spattering caused by recoil-pressure-induced keyhole instability (c1–c3) Core-ring beam at low energy: necking from insufficient overlap and unbalanced melt flow (d1–d3) Ring beam at low energy: track interruption (balling) resulting from severe instability and incomplete fusion. A detailed single-track analysis under related processing conditions is reported in the previous work [30].

fluctuation and significantly fewer spatters for the ring profile, confirming that lateral energy redistribution stabilizes the melt-pool boundary [30]. Consistent with these findings, Bauch et al. [42] demonstrated in Copper based study that ring-shaped beams lower vaporization by approximately 40 %, thereby reducing recoil pressure and enlarging the stable process window toward higher scan speeds and laser powers. The improved surface observed in the cube specimens therefore, originates from the more stable melt-pool behavior established during single-track formation. These findings are also consistent with other studies [44,45], which show that shaped beams such as ring or top-hat profiles enhance surface finish across various materials, including steels and fused silica, by reducing thermal gradients and

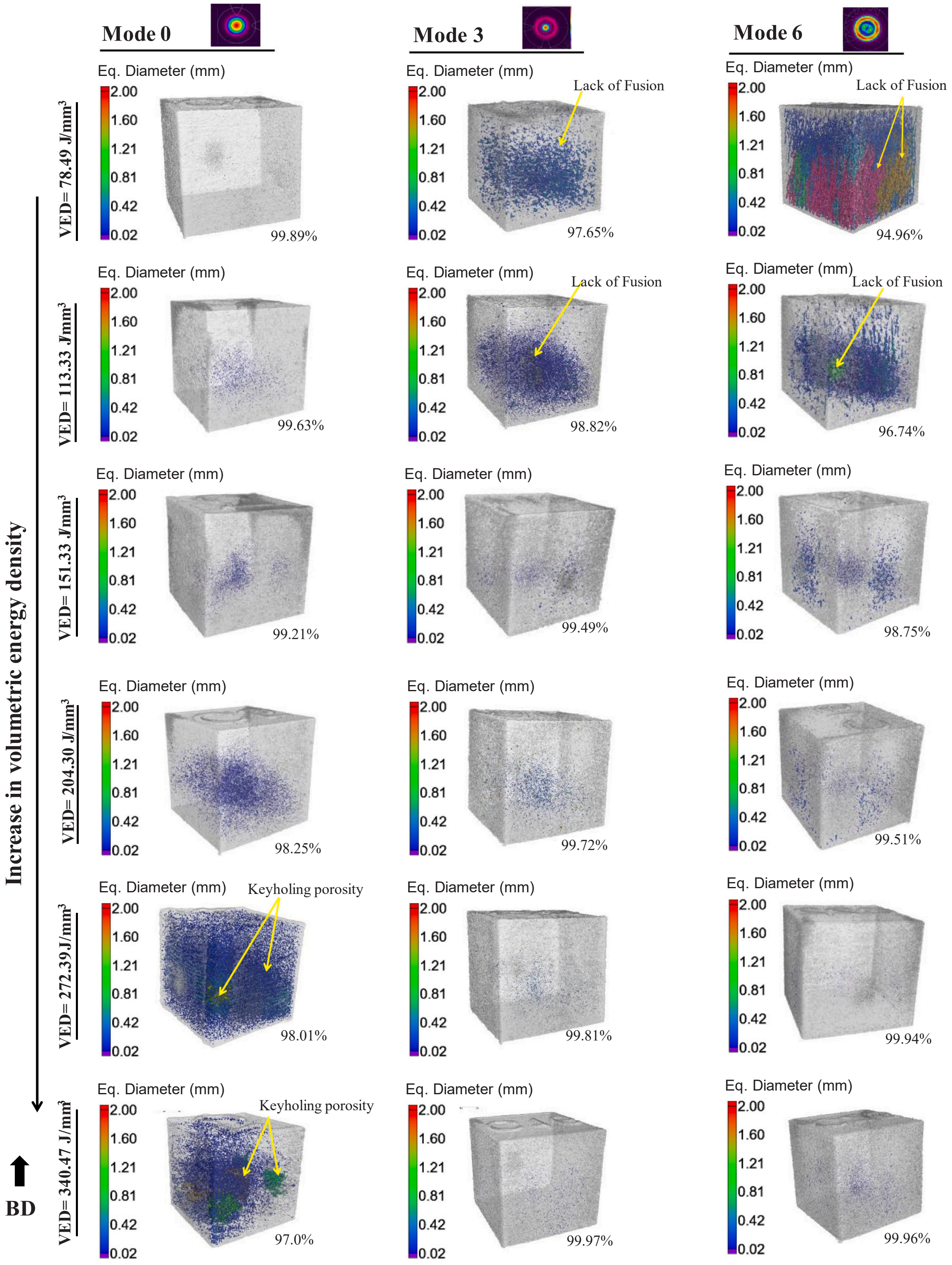

Fig. 6. 3D Micro-CT images showing the effects of beam shape and VED on porosity in PBF-LB/M Ti-6Al-4V. Columns represent beam shaping Modes (0, 3, 6), while rows display increasing VED levels (78.49–340 J/mm^3). The number below each image is the measured approximate density for that sample. The build direction (BD) is oriented upward in all views.

stabilizing melt-pool dynamics.

3.2. Effect of beam profiles on porosity and relative density

The formation of various pores, including metallurgical pores (small, near-spherical voids formed during solidification due to gas entrapment or micro-shrinkage), keyhole-induced porosity, and lack of fusion defects, plays a critical role in promoting cracking, increased surface roughness, and mechanical property degradation [46,47]. Fig. 6 presents Micro-CT 3D reconstructions of Ti-6Al-4V cube specimens, revealing differences in pore distribution, morphology, and overall porosity level among the various beam profiles and VED conditions. In this study, pores were classified based on their geometry and size: near-spherical pores below approximately 50 µm were considered gas-entrapped or metallurgical, while larger, elongated pores with higher aspect ratios were identified as lack-of-fusion or keyhole-related defects, consistent with common LPBF criteria. High-magnification views in Fig. 7 provide representative examples of these typical pore types.

As shown in Fig. 6, Mode 0 produces specimens with minimal porosity at lower VED levels (78.49–151.33 J/mm^3), containing only small, near-spherical pores typically 15–30 µm in diameter. As the VED exceeds 189.35 J/mm^3 and reaches 340.47 J/mm^3 (the highest energy used in this study), porosity rises sharply, with large, round pores that are mostly concentrated near the center, indicating keyhole-induced porosity caused by excessive energy input. This behavior results from deep melt pools and vapor cavity collapse, which trap gas and form large central pores, a phenomenon also reported in PBF-LB/M of Ti-6Al-4V single tracks and laser welding studies [47,48]. The thermal field within the cube is not uniform, as the central region experiences greater cumulative heating due to overlapping scan tracks and reduced lateral heat dissipation. This leads to higher steady-state temperatures and increased susceptibility to keyhole instability. Similar thermal accumulation behavior has been observed in numerical and experimental LPBF studies, where the interior of the cubic builds retains heat more effectively than the edges [49]. Furthermore, in situ synchrotron imaging has shown that keyhole collapse and bubble entrapment preferentially occur near the melt-pool center, where local flow velocity and cooling rate are relatively low, resulting in central pore retention [50]. However, this tendency is not uniform across all specimens. In most cases (particularly in ring beam profiles), pores are more randomly distributed or appear near the edges, while central clustering is more pronounced in Mode 0, where keyhole instability is promoted by the higher peak intensity of the Gaussian beam.

Fig. 9(a1–a3) presents SEM cross-sections of Mode 0 specimens, supporting the interpretations drawn from the micro-CT analysis. These images reveal pore features consistent with both lack-of-fusion defects and gas-induced porosity, aligning well with the observations from the 3D reconstructions. In Fig. 10, the variation in porosity and relative density observed for Mode 0 further supports this trend. At the lowest VED level (78.49 J/mm^3), samples exhibit high relative density (up to 99.89 %) with minimal porosity. However, as the VED increases, relative density declines sharply, reaching as low as 96.83 %. Previous studies with a full Gaussian profile also show that elevated energy input deepens the melt pool and promotes keyhole instability, resulting in increased porosity and a corresponding reduction in part density at higher VED levels [51,52].

In samples produced with Mode 3, pore formation is more pronounced at lower VED levels, as indicated by increased pore concentration and larger pore sizes (ranging from 51 to 100 µm). As the VED increases to $\geq$ 151.33 J/mm^3 , the porosity volume decreases markedly, yielding nearly pore-free cross-sections, as observed in the micro-CT

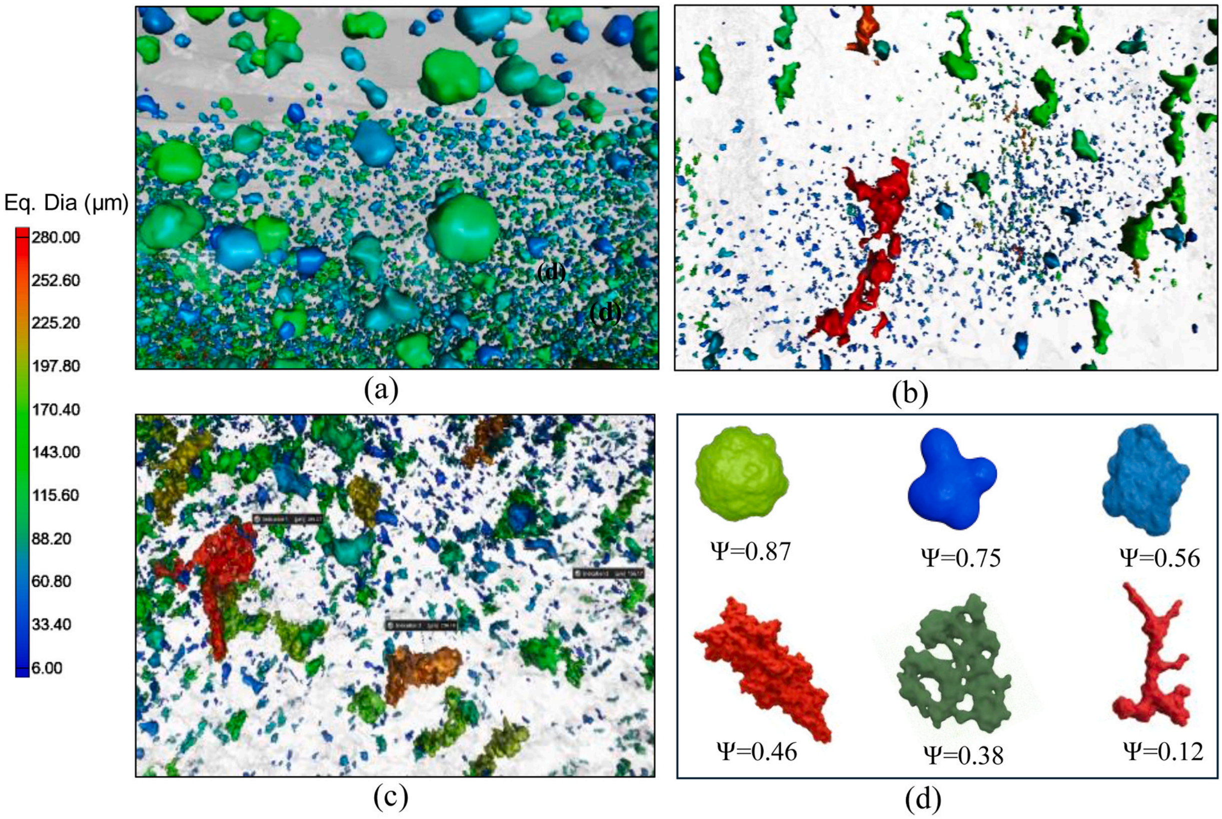

Fig. 7. High-magnification Micro-CT 3D reconstructions showing representative pore morphologies in Ti-6Al-4V cubes produced by different beam profiles at a VED of 204.30 J/mm^3 : (a) Mode 0, (b) Mode 3, and (c) Mode 6. (d) Examples of typical pore shapes extracted from the dataset, with their corresponding approximate sphericity (Ψ) values.

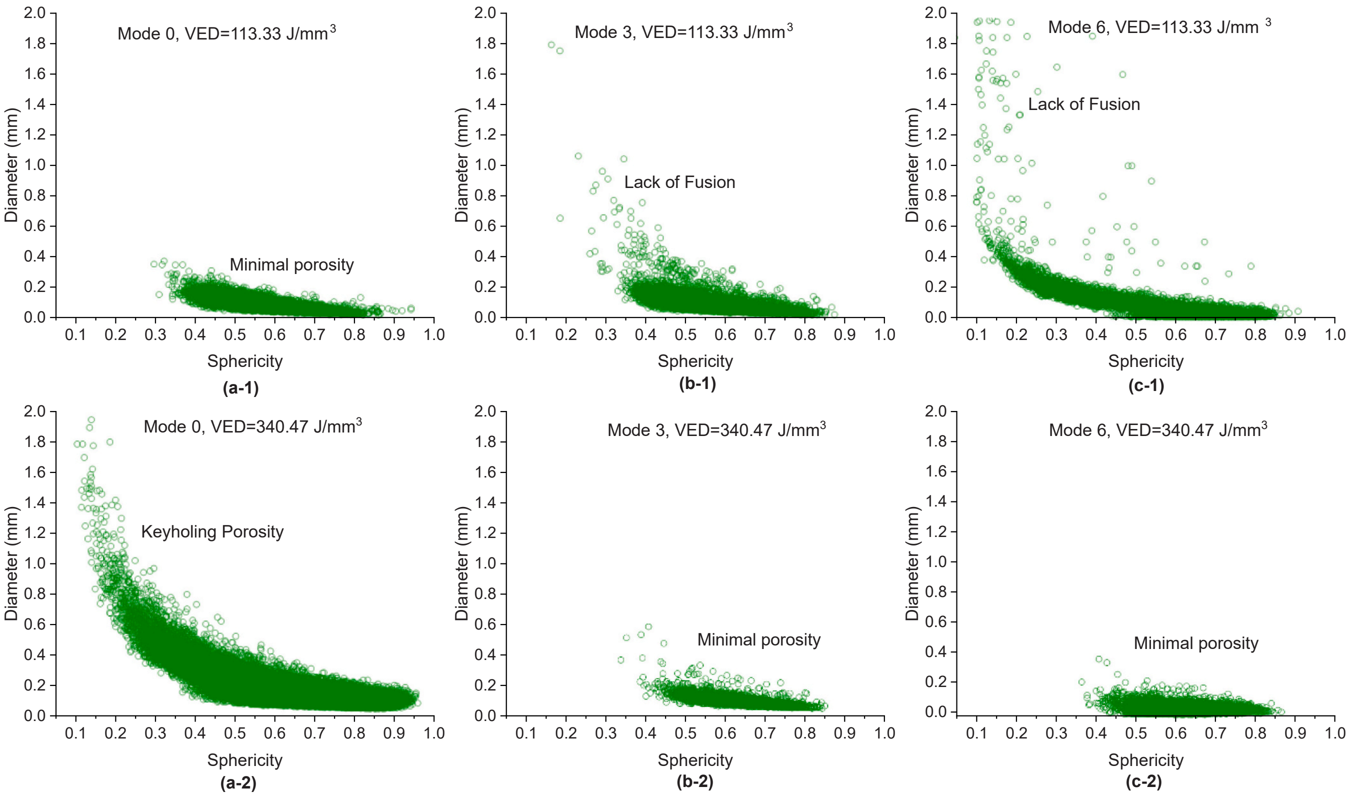

Fig. 8. Sphericity–diameter distribution of pores detected by micro-CT for the different beam modes and energy inputs: (a1—c1) low VED (113.33 J/mm^3) and (a2—c2) high VED (340.47 J/mm^3). Mode 0 shows minimal porosity at low VED but keyholing porosity at high VED. Mode 3 and Mode 6 exhibit lack-of-fusion porosity at low VED, while high VED conditions significantly reduce pore size and improve sphericity.

reconstructions of the cubes (Fig. 6 under Mode 3) and the polished SEM sections (Fig. 9b). The remaining small spherical pores in the CT images are presumed to be gas-induced. However, due to the voxel resolution limit of approximately 15 μm, smaller gas-related metallurgical pores typical of PBF-LB/M processes are likely below the detection threshold of this CT analysis. Pores detected near the resolution limit (often <10–15 μm) are likely minor artifacts identified by the software rather than actual voids within the material. Moreover, such features mostly do not reflect meaningful porosity and are unlikely to influence the overall density or structural integrity of the layers. Similar trends are observed in Mode 6 with variation in VEDs, although the severity of lack of fusion formation is slightly higher due to insufficient powder fusion. These observations are further supported and quantitatively validated by the sphericity–diameter distribution plots in Fig. 8, which highlight the progression from minimal porosity to severe keyholing in Mode 0, and from lack-of-fusion to minimal porosity and near-full densification in the ring beam profiles.

More specifically, Mode 6 samples show a high concentration of porosity at lower VEDs (ranging from 78.49 J/mm^3 to 151.33 J/mm^3), with a dense distribution of irregular pores indicative of LoF defects caused by insufficient energy input. This LoF porosity is particularly pronounced at the lowest VED of 78.49 J/mm^3 and is clearly visible along the build direction, as shown in Figs. 6 and 9(c) under Mode 6. The ring-shaped beam profile, characterized by a small central irradiance and broader energy distribution, tends to produce shallower, conduction-mode melt pools under low VED conditions [53,54]. At lower VED (here is 78.49 J/mm^3), Mode 6 produces a wider melt pool overall but with reduced energy intensity at the center, as observed in the previous study on single tracks [30]. Combined with the fixed hatch spacing, this leads to insufficient melt pool overlap between adjacent tracks within the same layer, leaving unbonded regions that form inter-track LoF pores. These pores are consistently located near the center of the cubes and appear vertically aligned in both CT and SEM images because the overlap gaps reoccur systematically in similar regions in each layer, despite the scan strategy rotation, due to the unchanged hatch distance relative to the melt pool shape formation. However, as the VED increases, a significant reduction in porosity volume is observed for Mode 6, as shown in the CT images (Fig. 9 under Mode 6, and the corresponding SEM images in Fig. 9 (c2-c3). In contrast to Mode 0, the porosity distribution becomes sparser, resulting in pore-free layers at the higher VED levels. This trend indicates that Mode 6 is highly effective at higher VEDs (up to 340.47 J/mm^3), resulting in controlled porosity and inclusions, which in turn lead to a smoother surface and a part density of up to 99.96 %, as illustrated in Fig. 10. The as-built samples reaching a relative density above 99.95 % were regarded as fully dense, consistent with previous studies [55]. However, these results also showed that achieving similar densification levels requires distinct energy inputs for each beam profile. The higher nominal VEDs required for Modes 3 and 6 primarily compensate for the redistributed laser energy across the beam cross-section, where the local peak intensity and effective energy input are lower than those of a Gaussian beam. As a result, the higher nominal energy input does not reflect greater total energy consumption but rather ensures equivalent local heating and complete powder melting. Despite the slightly higher nominal input, the ring-dominated profiles exhibited enhanced process stability and reduced keyhole-induced porosity, showing a practical balance between energy use and build quality.

3.3. *Microstructure and phase evolution*

The microstructure of Ti–6Al–4 V is influenced by its thermal history, which determines the transformation of the high-temperature β phase into various α-phase morphologies, including fine acicular α (commonly referred to as α′ martensite under rapid cooling), α-colonies,

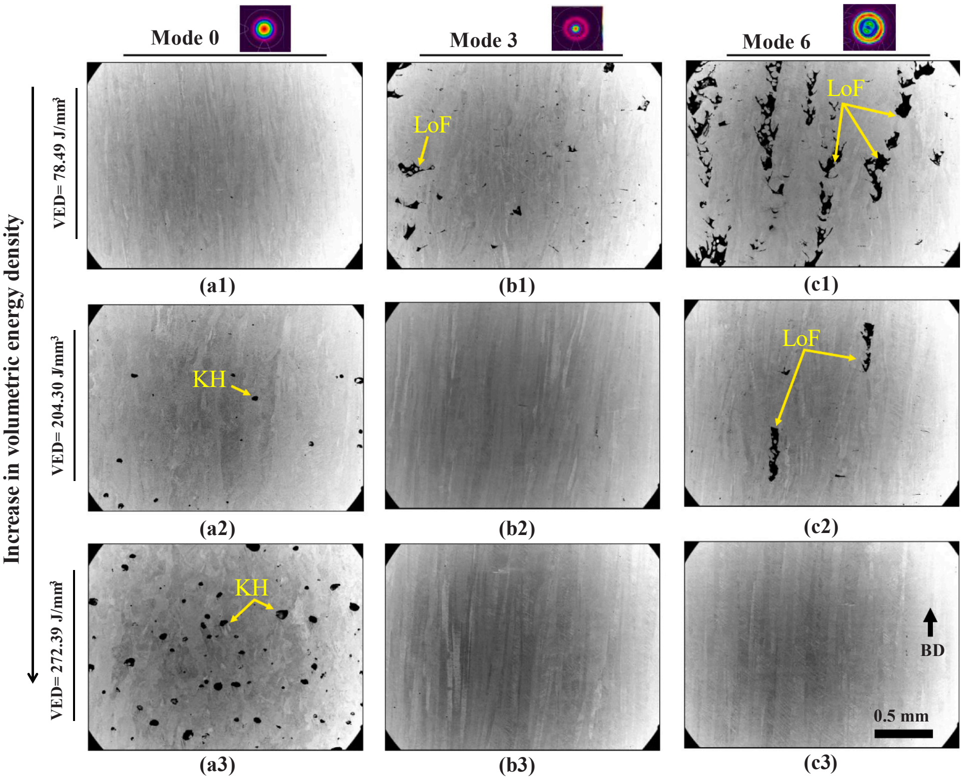

Fig. 9. SEM images of Ti-6Al-4V cubes produced with different beam profiles. Mode 0 (a1–a3), Mode 3 (b1–b3), and Mode 6 (c1–c3) at increasing VEDs. At low VED (78.49 J/mm^3), Modes 3 and 6 exhibit irregular lack-of-fusion (LoF) pores, while Mode 0 remains mostly dense. At increased VED (up to 204.30 J/mm^3), Mode 0 shows rounded keyhole (KH) pores, whereas Modes 3 and 6 still display some signs of LoF porosity. At the higher VED (272.39 J/mm^3), Mode 0 exhibits concentrated KH pores near the center of the build, while Mode 6 appears nearly pore-free. The build direction (BD) is indicated by the arrow, applied to all images.

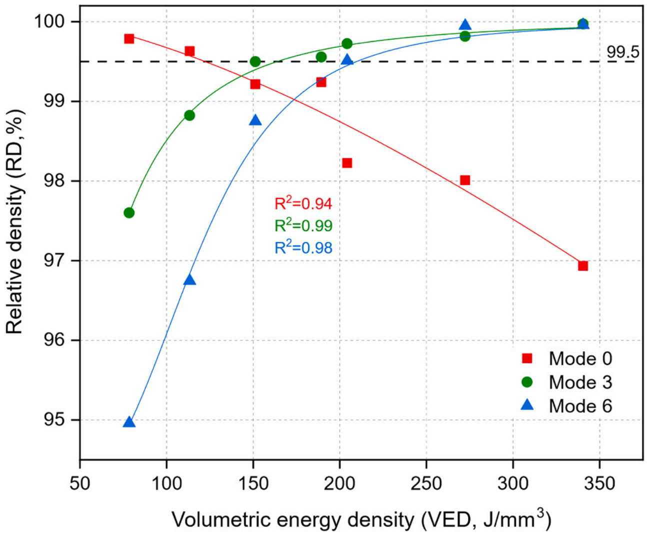

Fig. 10. Relative density of Ti-6Al-4V cubes as a function of VED for different beam profiles. Modes 3 and 6 reach nearly full density (~99.97 % and 99.96 %, respectively) at higher VED (340.47 J/mm^3), whereas Mode 0 shows a gradual decline due to keyhole-induced porosity. The dashed line at 99.5 % indicates the reference for full densification. The measurement uncertainty is estimated at ±0.3 %.

and may also result in a small fraction of retained β phase at room temperature. The prior β-grain structure, formed during solidification, further influences the morphology and spatial distribution of the transformed α-phase [56,57]. Fig. 11 illustrates the evolution of the prior-β grain morphology in response to variations in beam shaping and laser energy density. At the lower VED of 78.49 J/mm^3 , all beam modes exhibit narrow and continuous columnar prior-β grains aligned along the build direction (BD), containing α′ martensitic colonies and distinct α grain boundaries (GB), showing highly directional solidification driven by strong thermal gradients and stable melt pool conditions. The vertical alignment of columnar prior-β grains along the build axis results from the re-melting of the previous layer and directional solidification, driven by the temperature gradient established during the melting process [58,59]. As the molten material cools, it solidifies from the edges to the center, resulting in the formation of grains that align with the direction of heat flow, which is typically parallel to the build direction, as also reported in previous studies [60,61].

As the energy input increases (≥150 J/mm^3), a clear transformation in prior-β grain morphology is observed across all beam modes. In Mode 0, the previously continuous prior-β grains lose their full continuity and change into segmented or partially interrupted columnar structures, with grains exhibiting limited growth lengths and local misorientations along with other local defects, including porosity, likely caused by increased melt pool instability and altered solidification dynamics, which are more obvious at 204.30 J/mm^3 and higher, as shown in Fig. 11 (a2-a3). This segmentation is attributed to increased melt pool instability and complex thermal convection, which disturb steady epitaxial β-grain growth and promote local re-nucleation under fluctuating solidification conditions. Similar energy-related effects on grain morphology transitions have been observed in high-power deposition processes, where excessive energy input lowers cooling rates and alters solidification dynamics, leading to coarser or more variable prior-β grain structures. Comparable high-energy phenomena were reported in Ti-6Al-4V deposition studies, where excessive energy input alters the thermal gradient and cooling rate, leading to coarser or more variable prior-β grain structures and modified α-lath morphologies [62,63]. Additionally, nearly spherical pores are observed, primarily attributed

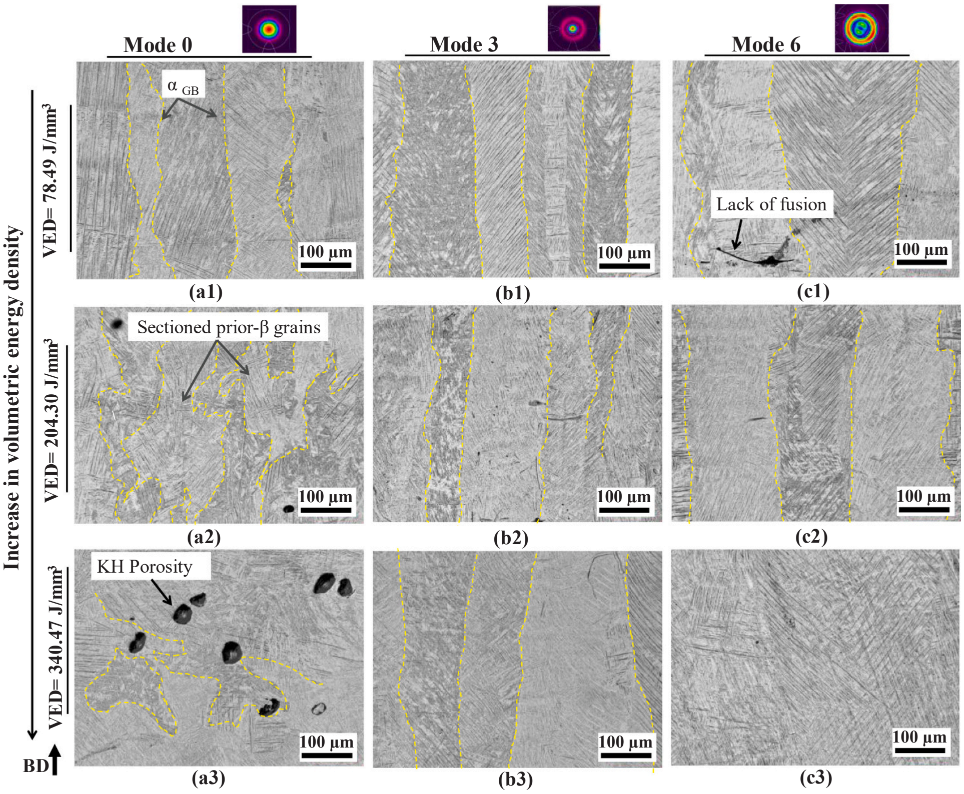

Fig. 11. SEM images showing the evolution of prior-β grain morphology in Ti-6Al-4V fabricated with different beam shaping modes (Mode 0 (a1–3), Mode 3 (b1–b3), and Mode 6 (c1–c3)) at varying volumetric energy densities (78.49–340.47 J/mm^3). The figure illustrates the transition from narrow, continuous columnar grains at lower energy input to segmented structures in Mode 0 and to wider columnar grains in the ring profiles at higher energy densities. The same build direction (BD) applies to all images.

to keyholing and vaporization caused by the high energy input, as demonstrated in the previous sections. In contrast, both Modes 3 and 6 exhibit continuous columnar prior-β grains with well-defined grain boundaries. However, these grains are noticeably wider and more laterally extended at higher energy inputs. This change in grain size and morphology reflects the broader, less intense central energy distribution of the ring-shaped beams, which reduces thermal gradients and suppresses localized overheating. As a result, more stable melt pool

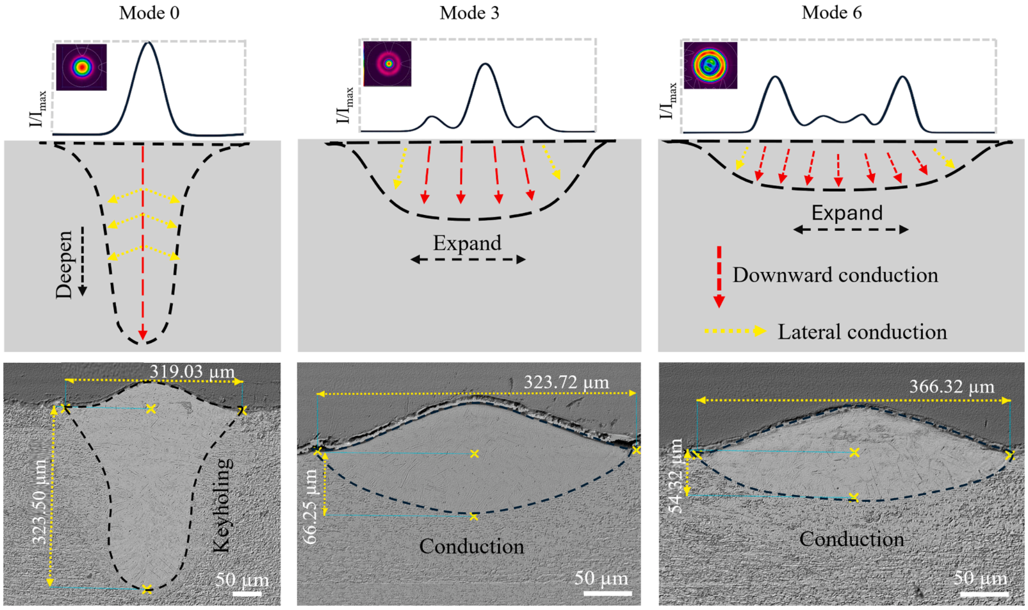

Fig. 12. Normalized intensity profiles (I/I$_{max}$, defined as local intensity divided by peak intensity, illustrating relative energy distribution), schematic melt pool shapes with dominant heat conduction directions, and corresponding cross-sectional geometries for Mode 0, Mode 3, and Mode 6 beams in Ti-6Al-4V single tracks. Mode 0 forms a deep keyhole-shaped pool with dominant downward conduction. Mode 3 produces a moderately wide pool with balanced heat flow and continuous columnar grains, while Mode 6 yields the widest, shallowest pool that supports aligned β-grain growth with minimal boundary disruption.

dynamics and continuous directional solidification are maintained, minimizing grain fragmentation typically associated with melt pool fluctuations. These observations support the conclusion that the ring-shaped profiles in Modes 3 and 6 facilitate a more uniform energy input and enhanced control during solidification. Notably, at the higher energy density ($\geq$ 204.30 J/mm^3), Mode 6 promotes the formation of distinctly wider and more flattened prior-β grains (Fig. 11(c3)) compared to Mode 3, likely due to its higher ring intensity ratio, which further broadens the melt pool and extends the solidification front. Schematic Fig. 12 provides a visualization of how the energy distribution of different beam profiles governs heat conduction and melt pool geometry in single tracks, offering the underlying explanation for the observed differences in grain morphology.

Following prior-β grain formation, the transformation into the α-phase was examined to assess the combined influence of beam shape and varying energy densities on the morphology of the α′ martensitic laths, as shown in Fig. 13. This martensitic structure is inherently hierarchical, so a mixture of larger (primary) and finer (secondary, tertiary) laths is naturally present. Overall, the morphology remains dominantly martensitic, with no obvious signs of decomposition or major structural changes across the tested conditions. While differences in lath orientation, thickness, length, and spatial distribution are observed with varying VED and beam profile, these variations remain within the typical range reported for PBF-LB/M-produced Ti-6Al-4V [64,65]. At low VED (78.49 J/mm^3), all beam shapes produced fine, densely packed acicular α′ laths intersecting at various angles, reflecting multi-variant martensitic transformation within the prior-β grains. With increasing VED (up to 204.30 J/mm^3), Mode 0 shows a typical mix of fine and slightly coarser laths due to thermal heterogeneity, while Modes 3 and 6 maintain a more uniform α′ structure. At the highest energy density (340.47 J/mm^3), Mode 0 shows locally coarser laths and signs of initial decomposition. While the dark contrast regions in the BSE images may partly result from α-phase orientation, their consistent occurrence only in specimens with pronounced keyhole porosity suggests that pore-related surface relief or etching effects may also contribute, as confirmed by the above-reported results from CT and SEM cross-sections. Modes 3 and 6 maintain a fully martensitic structure with fewer visible defects, and although minor differences in lath alignment appear, the microstructure remains comparable across all conditions.

3.3.1. *EBSD analysis of prior-β grain morphology and α′ martensite evolution*

The EBSD inverse pole figure (IPF) maps of the reconstructed prior-β grains (Fig. 14) provide additional insight into the evolution of grain morphology, crystallographic orientation, and phase distribution across varying beam profiles and energy inputs, complementing the observations in Fig. 11. For conditions exhibiting higher overall porosity, EBSD scans were conducted on locally dense regions to ensure accurate texture analysis and avoid artefacts associated with large LoF pores. At lower energy density ($\leq$130.81 J/mm^3), all beam modes exhibit elongated, directionally aligned columnar prior-β grains along the BD. The IPF maps reveal fine α′ laths oriented within these columnar grains, with Mode 6 showing particularly stronger alignment and more uniform crystallographic orientation than Mode 0, reflecting stable directional solidification. In all modes, nearly complete transformation into α-phase occurs, with no retained β detected within the resolution of the measurement. As energy density increases, distinct differences emerge between the beam modes, which are particularly notable at $\geq$ 151.33 J/mm^3 . In Mode 0, increasing VED leads to progressive grain fragmentation, reduced grain continuity, and significant misorientation. The IPF maps show a breakdown in prior-β grain alignment and increased fragmentation at higher VEDs (up to 204.30 J/mm^3 in Fig. 14),

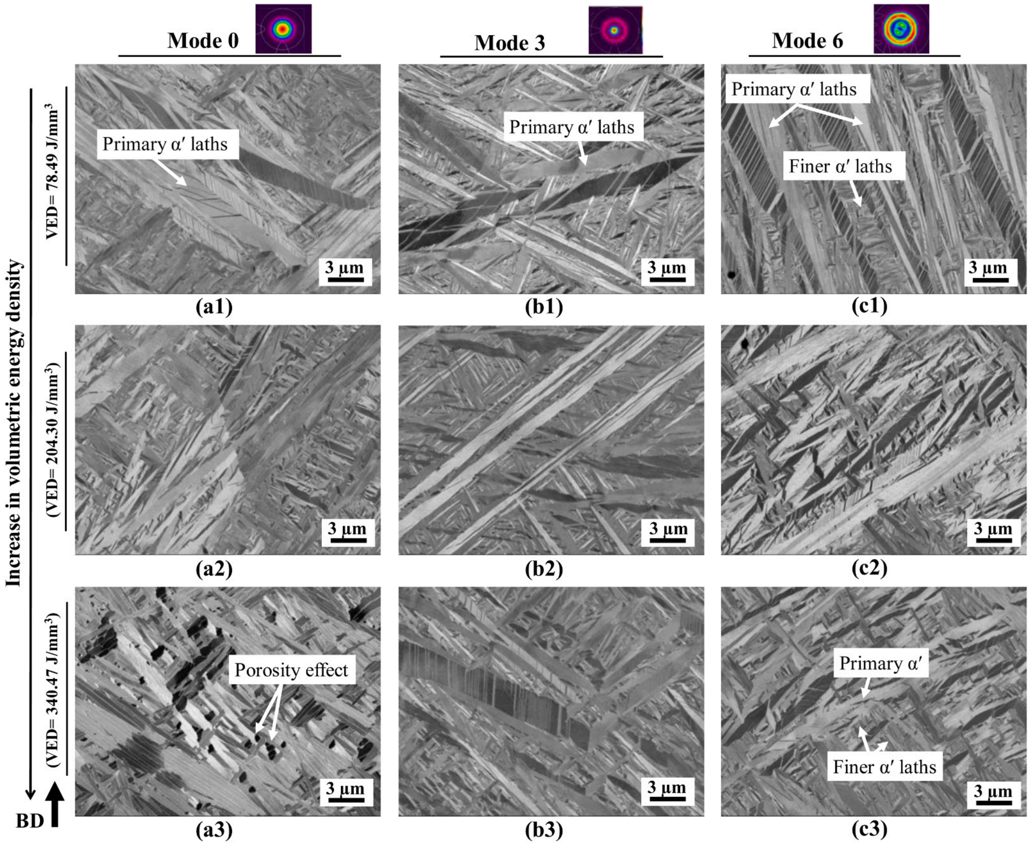

Fig. 13. SEM micrographs of Ti-6Al-4V (α′ martensitic morphology) manufactured using the three beam profiles (Mode 0 (a1–a3), Mode 3 (b1–b3), and Mode 6 (c1–c3)) and varying VEDs (78.49 J/mm^3–340.47 J/mm^3). All images were acquired from the central region of longitudinal cross-sections. The white arrow indicates the build direction (BD), applicable to all images.

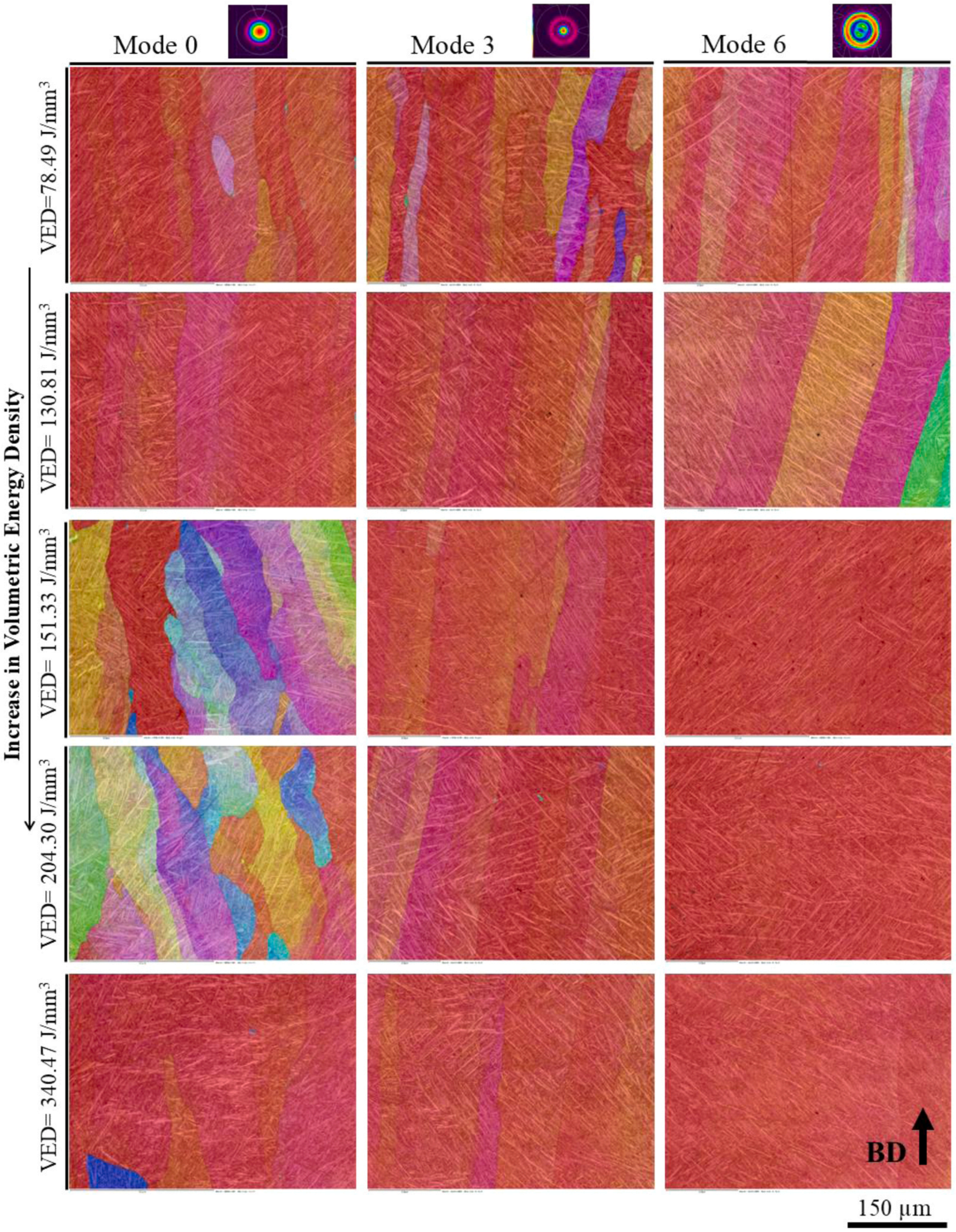

Fig. 14. EBSD IPF orientation maps of reconstructed prior-β grains in Ti-6Al-4V samples processed with different beam shapes (Mode 0, Mode 3, Mode 6) across increasing volumetric energy densities (VEDs: 78.49–340.47 J/mm^3).

indicating a loss of directional solidification and greater thermal fluctuation during melt pool evolution. However, the specimen processed at 340.47 J/mm^3 deviates from this trend. The excessive energy input likely transitions the process into a high-energy regime similar to Directed Energy Deposition (DED) [66,67] or Wire and Arc Additive Manufacturing (WAAM) [68,69], where deep melt pools, strong thermal gradients, and slower cooling promote columnar prior-β grain regrowth and a pronounced ⟨001⟩ texture rather than further fragmentation.

In contrast, Modes 3 and 6 maintain continuous and aligned prior-β grains with less misorientation, indicating a more stable melt pool and solidification front throughout the VED range. Mode 3 maintains a relatively uniform and continuous grain growth with moderate widening and smaller misorientation in the BD. Among the beam profiles, Mode 6 exhibits the most stable grain morphology at high energy densities, with continuous and uniformly aligned prior-β grains, as seen in the EBSD maps (Fig. 14 under Mode 6) at 340.47 J/mm^3. The consistent coloration and a dominant growth direction indicate strong crystallographic alignment and reduced grain boundary disruption. This stability results from the ring-shaped beam profile, which produces a wider, shallower melt pool (as illustrated in Fig. 12) that supports lateral grain growth and minimizes thermal gradients. In addition, the arrangement of α′ martensite laths also reflects the differences in prior-β grain continuity. In Mode 0, where grain fragmentation is more prevalent, the α′ laths tend to grow within individual prior-β grains, mostly terminating at GB due to the interrupted grain structure (in all VED conditions). In contrast, Modes 3 and particularly Mode 6 display well-aligned prior-β grains, allowing the α′ laths to grow more consistently across broader regions, mostly observed extending smoothly from one grain into another, following the preserved crystallographic orientation established during solidification.

The development of phases and crystallographic texture in PBF-LB/M Ti-6Al-4V is directed by thermal gradients, solidification behavior, and transformation kinetics. In line with previous studies [70,71], these results reveal that while VED remains the primary factor influencing prior-β grain structure and α/α′ morphology through its control of cooling rates, beam shaping also plays a significant and independent role. Mode 0’s Gaussian beam generates steep gradients and rapid cooling, leading to fragmented β grains and fine α′ martensite. In contrast, Modes 3 and specifically Mode 6 promote broader, stable melt pools, enabling continuous β grains and uniform α′ lath growth across grain boundaries, aligned with the preserved crystallographic orientation [72,73].

The evolution of crystallographic texture with varying VED and beam shaping is assessed through {100} β pole figure analysis, as shown in Fig. 15. At low energy density (≤ 130.81 J/mm^3), all beam modes exhibit relatively weak textures, reflecting the early stages of columnar grain formation. Mode 6 shows slightly stronger texture at this stage (with a maximum pole density of 27.53 m.r.d), likely due to improved melt pool stability provided by the ring-shaped beam profile even at lower thermal input. To clearly illustrate the overall trend, Fig. 16 plots

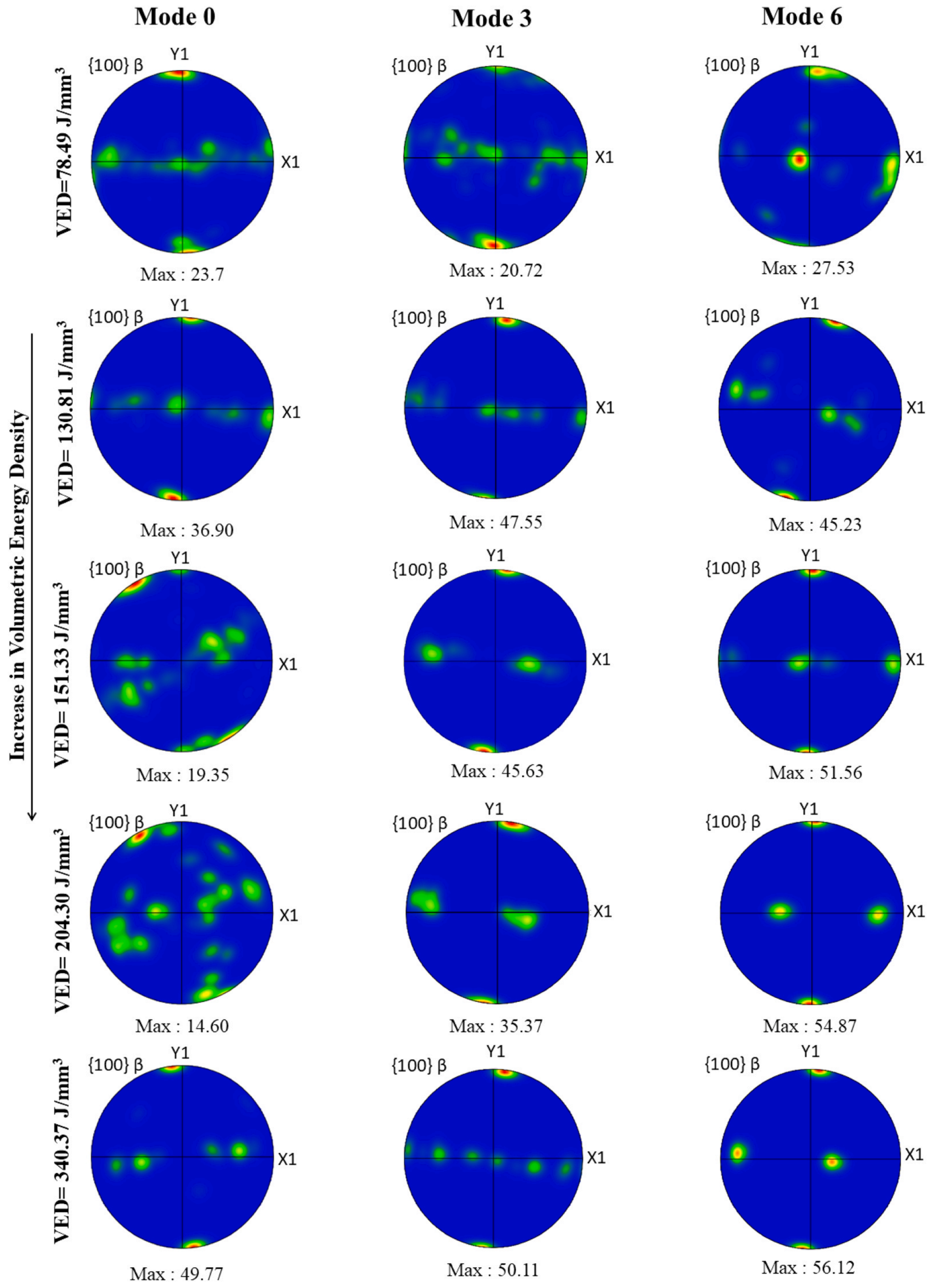

Fig. 15. Pole figures corresponding to the EBSD-based reconstructed prior-β grains, showing crystallographic texture evolution in Ti-6Al-4V with varying beam shapes and VEDs.

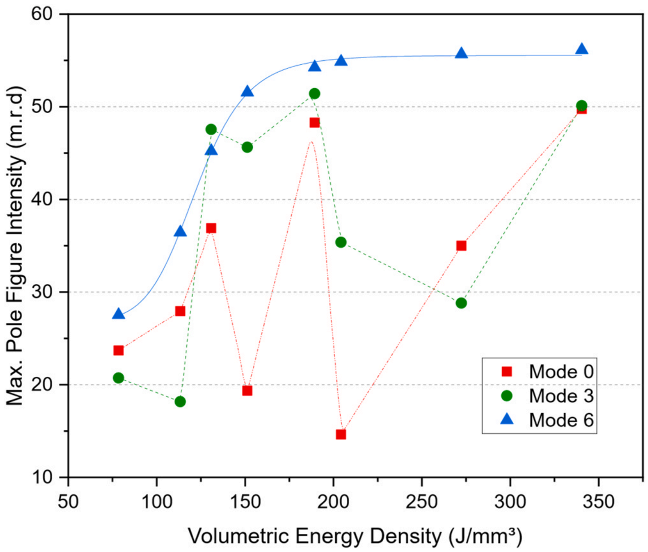

Fig. 16. Maximum {100} pole figure intensities for the different beam profiles and VED levels. Each point represents an individual EBSD scan. Dashed lines indicate general trends and are not intended to represent interpolated values. Mode 6 follows an exponential saturation fit, Modes 0 and 3 are LOESS guides to the eye.

the maximum pole figure intensity values extracted from Fig. 15, showing how texture strength gradually changes with VED and varies between beam modes. As energy density rises, distinct differences between the beam modes become evident. In Mode 0, texture intensity initially increases at moderate VED (130.81 J/mm^3), consistent with grain elongation and some alignment along the build direction. However, further increases in VED (151.33–204.30 J/mm^3) lead to rapid texture weakening, reflecting the grain fragmentation and misorientation observed in the EBSD orientation maps. The apparent increase in maximum pole intensity value at the highest VED (340.47 J/mm^3) in Mode 0 reflects the development of a stronger ⟨001⟩ texture associated with the regrowth of columnar β-grains (as observed in Fig. 14) under excessive energy input, rather than random accumulation of misoriented grains.

Compared to the Gaussian beam, beam shaping in Modes 3 and 6 produces more stable and consistently developed textures over the full range of energy densities. Mode 3 apparently maintains a strong and consistent texture with increasing VED, reflecting its ability to stabilize melt pool geometry and sustain continuous columnar growth. Mode 6 exhibits the most stable texture intensities across all processing conditions (the gradual increase from lower to higher VED), reaching a maximum pole intensity of 56.12 at the highest VED. This texture stability is attributed to the wider, shallower melt pool geometry produced by the ring-shaped beam, which minimizes thermal instabilities and grain misorientation while maintaining continuous prior-β grains and promoting highly directional solidification, even at elevated energy inputs. These results further emphasize that, while VED primarily determines the overall thermal input, beam shaping strongly influences texture formation by stabilizing melt pool dynamics and enabling more consistent directional solidification, which promotes the development of well-aligned grain structures. Although clear differences in microstructure and texture evolution are observed between the beam modes and energy inputs, the underlying causes and the detailed mechanism of the development of phases and crystallographic texture in PBF-LB/M remain complex, involving multiple interacting factors that are not yet fully understood.

3.4. Process interpretation based on normalized energy input

To further interpret the beam-shaping effects beyond the volumetric energy framework, the process behavior was also analyzed using the areal energy density (AED), calculated based on the width of the measured melt pool. Figs. 17 and 18 compare the surface roughness and relative density as a function of AED and its normalized form, using the same dataset as the VED analysis but reinterpreted under the areal energy framework. The normalization of AED is carried out using a common reference point where all beam profiles exhibited comparable values, corresponding to $S_a \approx 14\ \mu m$ for surface roughness and $RD \approx 99.5\%$ for relative density. As shown in Fig. 17(a), Mode 0 produces relatively lower surface roughness (Sa) at a smaller AED, owing to its concentrated peak intensity that promotes efficient initial melting. However, as the areal energy increases, the roughness rises steadily, indicating excessive local heating and unstable melt-pool dynamics. In contrast, Mode 3 and Mode 6 beams exhibit a clear decrease in Sa with increasing AED, followed by a plateau (Sa ≈ 11–12 μm), suggesting that distributed energy input promotes stable melting and smoother surface formation. After normalization (Fig. 17 (b)), all curves intersect near $AED_n = 1$, where $S_a \approx 14\ \mu m$. Below this point, the Gaussian beam performs slightly better, while above it, both ring-shaped beams maintain low roughness, demonstrating their improved thermal stability and reduced sensitivity to excessive energy input.

A similar trend is observed for relative density (RD) in Fig. 18 (a-b). At low AED, all beams show a rapid rise in density as lack-of-fusion porosity is eliminated. Mode 0 produces higher density at relatively lower AED and declines at higher input, indicating keyhole porosity. The ring and ring-core beams reach nearly full density (≈99.5–99.9 %) at moderate AED (≥1.7) and maintain it across a wide process window. The normalization (at RD = 99.5 %) aligns the full-density condition (AED_n=1) for all modes, allowing direct comparison of process robustness. The comparison becomes clearer, where for $AED_n \leq 1$, Mode 0 is stable, while the ring beam profiles are in the incomplete melting regime. For $AED_n \geq 1$, only the Gaussian profile loses density, whereas the ring-based beams remain fully dense and stable. Overall, these normalized comparisons highlight that beam shaping widens the stable processing window by balancing energy distribution within the melt pool. The Gaussian beam efficiently melts powder at low input but becomes unstable at higher energies, leading to rough surfaces and keyhole porosity. In contrast, ring and ring-core beams achieve smoother, denser, and more consistent surfaces within a broader energy range. Similar trends for surface roughness and density appeared in the VED-based analysis, as both metrics scale with the total energy input under otherwise identical process parameters.

Microstructural analyses of additional samples produced at equal and relatively lower and higher areal energy densities were performed to further elucidate the influence of beam shaping on grain morphology and crystallographic texture. At the lower AED of approximately 1.6 J/mm^2 (Figure S1 in the supplementary Data), all beam profiles yield elongated prior-β grains, similar to the trends observed in Fig. 14 for different VEDs. Mode 0 exhibits relatively narrow β grains and distinct keyhole-like boundaries, containing fine α′ martensite confined mostly within grain interiors. Mode 3 produces slightly wider and better-aligned β grains, with α′ laths extending across multiple β grain boundaries, suggesting improved melt-pool stability. In Mode 6, the β grains appear markedly wider and more uniformly oriented along the build direction, resulting in a flatter, lamellar morphology. The α′ laths are noticeably longer and more continuous, traversing several β grain boundaries in a diagonal arrangement, indicative of more homogeneous solidification. At the higher AED of 2.7 J/mm^2 (Figure S2 in the supplementary data), the same progression among beam profiles persists. Mode 0 develops segmented β grains with randomly oriented, fine α′ martensite, characteristic of locally unstable solidification. In contrast, Mode 3 reveals more aligned and continuous β grains, whereas Mode 6 produces a distinctly flat and highly oriented structure with thin,

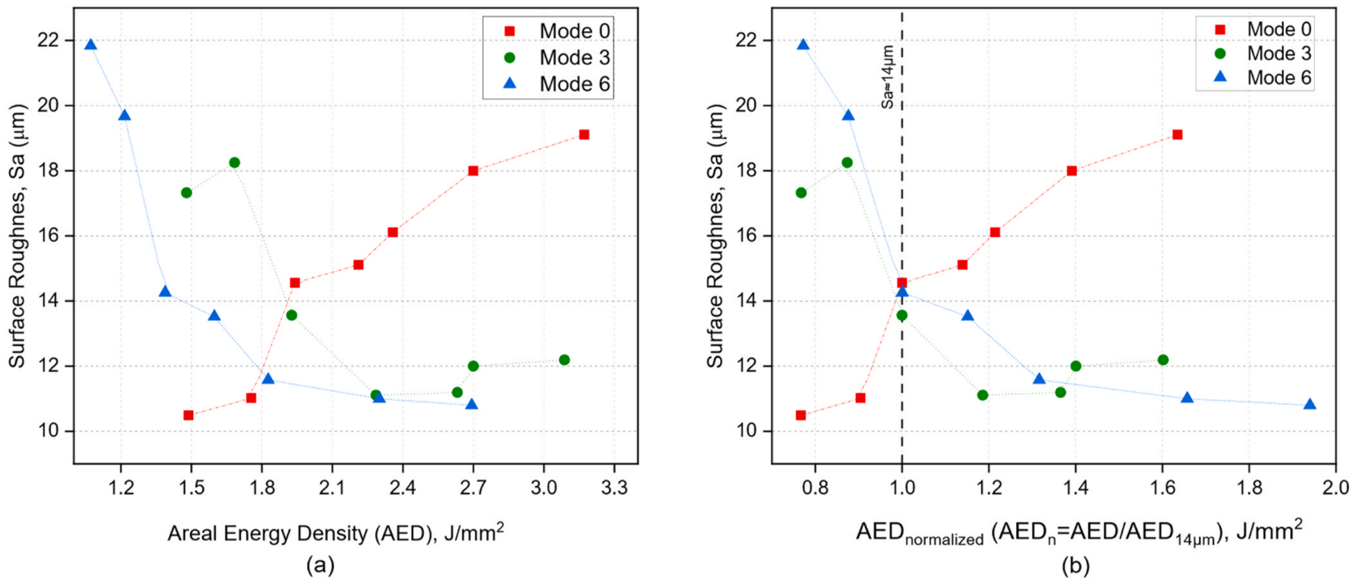

Fig. 17. Variation in surface roughness (Sa) with areal energy density (AED) for the different beam profiles. (a) actual AED values and (b) normalized AED_n values. The normalized plot highlights a converging roughness behavior around reference point $AED_n = 1$. Lines are shape-preserving interpolations to guide the eye. Here, $AED_{14\ \mu m}$ denotes the reference areal energy density corresponding to a surface roughness of approximately 14 μm.

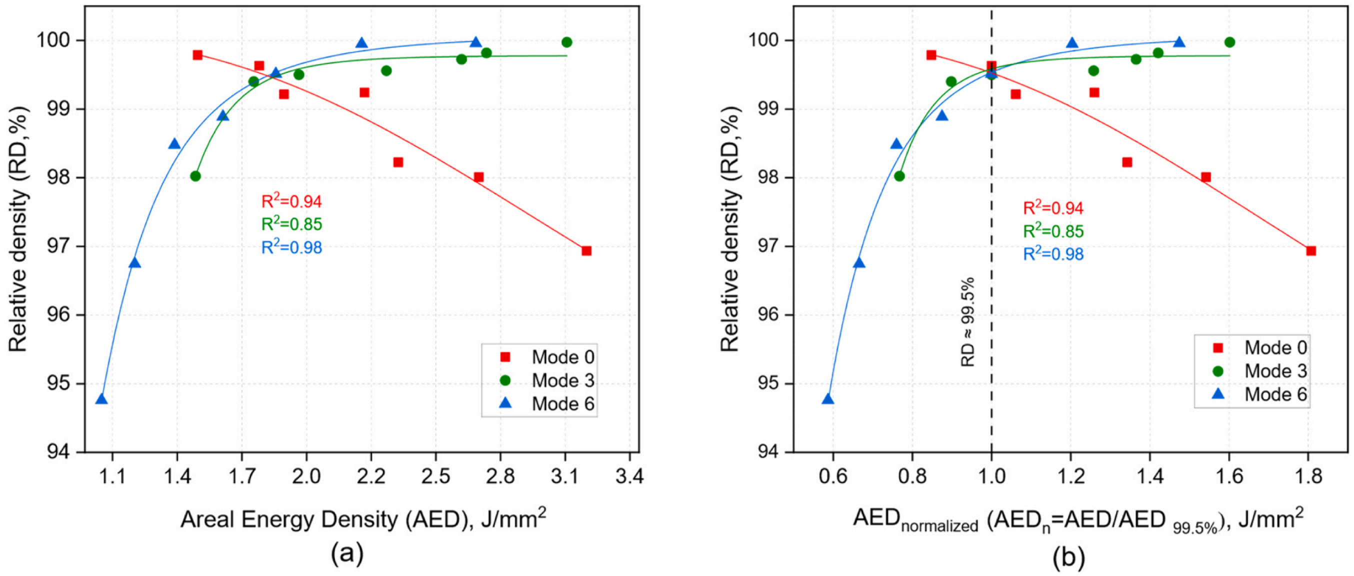

Fig. 18. Relative density of Ti-6Al-4V specimens fabricated with different beam profiles as a function of (a) AED based on measured melt-track width and (b) normalized areal energy density (AED_n). Here, $AED_{99.5\ \%}$ denotes the reference areal energy density corresponding to a relative density of 99.5 %, used for normalization of the AED value.

elongated α′ laths. The reconstructed β maps and {100}β pole figures at both AEDs consistently show an increase in maximum pole intensity from Mode 0 to Mode 6, reflecting the progressive enhancement in texture and grain alignment with the change in the beam profile. Overall, these results align closely with the VED-based findings, confirming that the influence of beam shape on melt-pool stability, grain refinement, and texture development remains consistent across both energy representations.

4. Mechanical properties

4.1. Microhardness

Vickers microhardness measurements conducted across multiple VED levels (78.49–340.47 J/mm^3) and different beam profiles (Mode 0 to Mode 6) revealed systematic trends influenced by both energy input and beam shaping. Fig. 19 summarizes the results based on 75 indentations per VED level, with 25 measurements performed for each beam mode. Overall, the microhardness values remained relatively consistent across the tested process window, mostly ranging between 370 HV and 400 HV. This small variation reflects the predominance of α′ martensite formation in all conditions, as confirmed by microstructure analysis, where high cooling rates consistently promote full martensitic transformation. While beam shaping significantly affects grain morphology, phase distribution, and porosity, its impact on microhardness remains limited in the as-built state due to the uniform presence of α′ martensite. At the lowest VED level (78.49 J/mm^3), Mode 6 exhibited the highest average microhardness (396.8 ± 13.4 $HV_{0.1}$),

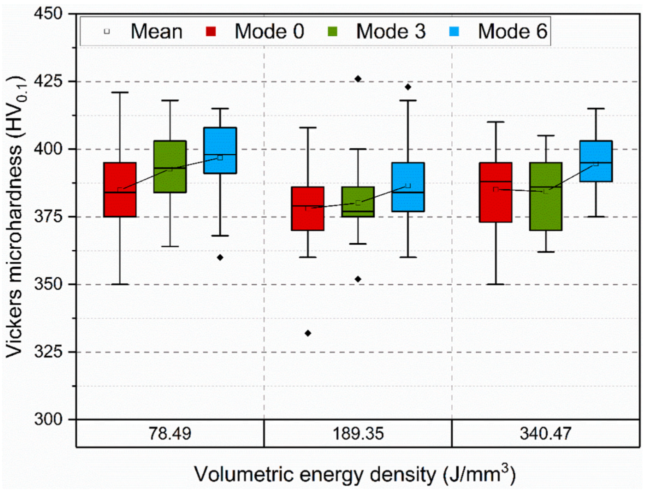

Fig. 19. Vickers microhardness ($HV_{0.1}$) results for the three different beam profiles (Mode 0, Mode 3, Mode 6) and VED levels (78.49 J/mm^3, 189.35 J/mm^3, 340.47 J/mm^3). Box plots show average values and standard deviations for each condition.

followed closely by Mode 3 (392.5 ± 13.7 $HV_{0.1}$), while Mode 0 showed a lower value of 375 ± 14.6 $HV_{0.1}$. This trend reflects the enhanced microstructural refinement induced by the ring-shaped beam, where a more uniform energy distribution promotes finer and more homogeneous α-phase formation. With increasing VED, the variation in microhardness across beam profiles becomes narrower, although Mode 6 consistently maintains slightly higher values (394.6 ± 11.1 $HV_{0.1}$) compared to Mode 0 (385.2 ± 17.7 $HV_{0.1}$). This reduced variation primarily reflects the predominance of α′ martensite under most processing conditions, with possible localized phase changes (e.g., early-stage decomposition) at higher VEDs, as suggested by microstructural observations. The comparatively higher fluctuations and standard deviations observed for Mode 0 at both low and high VEDs further indicate underlying microstructural inconsistencies.

4.2. Indentation-derived tensile properties

The indicative tensile properties derived from indentation analysis show clear and systematic relative trends for each beam shape with increasing VED (Fig. 20), which support the microstructure observations. In Mode 0, the average and estimated Ultimate Tensile Strength (UTS) gradually decreases from about 1176 MPa at 78.49 J/mm^3 to ~1085 MPa at 340 J/mm^3 , while the estimated Yield Strength (YS) similarly drops from 1055 MPa to 1022 MPa. In contrast, Mode 3 demonstrates a consistent increase in both strength indicators with rising VED, where UTS rises from ~1050 MPa to ~1159 MPa and YS from ~915 MPa to ~1052 MPa. Mode 6 shows the strongest apparent dependence on energy density, with UTS increasing from ~974 MPa at 78.49 J/mm^3 to ~1192 MPa at 340 J/mm^3 , while YS rises from ~787 MPa to ~1000 MPa. The ductility (D) follows distinct trends where for Mode 0, D initially increases up to 20.5 % at 189.35 J/mm^3 before declining to 14.1 % at 340.47 J/mm^3 . For Mode 3, D decreases from 23 % to 13 % as VED rises; while for Mode 6, D starts high (~29 %) and stabilizes to ~21 % at higher VEDs. These values are intended for relative comparison only, based on inverse FEM correlation to Ti-6Al-4V tensile data in compliance with DIN SPEC 4864, and do not replace standard tensile tests, as described in the methods Section 2.3.

4.2.1. Indentation-derived stress-strain behavior

Fig. 21 shows the indicative stress–strain trends that support the evolving tensile behavior inferred for each beam shaping condition. Mode 0 shows higher strength but limited ductility (D ~14 %) and more scatter, reflecting grain fragmentation and higher porosity at VED ≥ 150 J/mm^3 . Mode 3 indicates improved balance between strength and ductility (D 14–21 %) as grain continuity improves and the melting condition is improved. Mode 6 demonstrates the most favorable trend, with initially high ductility at low VED, reducing and stabilizing to ~21 % at 340.47 J/mm^3 , showing uniform stress–strain profiles with smooth yielding. Overall, these indicative stress–strain trends reflect the influence of beam shaping and VED on melt pool stability and grain structure evolution, supporting the observed microstructural trends.

5. Process-structure-property correlation

The variations in mechanical behavior across beam profiles and energy inputs highlight the interconnected effects of melt pool dynamics, surface quality, porosity evolution, and microstructural development. At lower VED using Mode 0, rapid cooling promotes the formation of fine α′ martensite, yielding relatively high hardness and strength. As VED increases, melt pool instability and keyhole formation drive surface roughness, grain fragmentation, and central keyhole porosity. These defects, together with elevated residual stress, reduce UTS and YS and

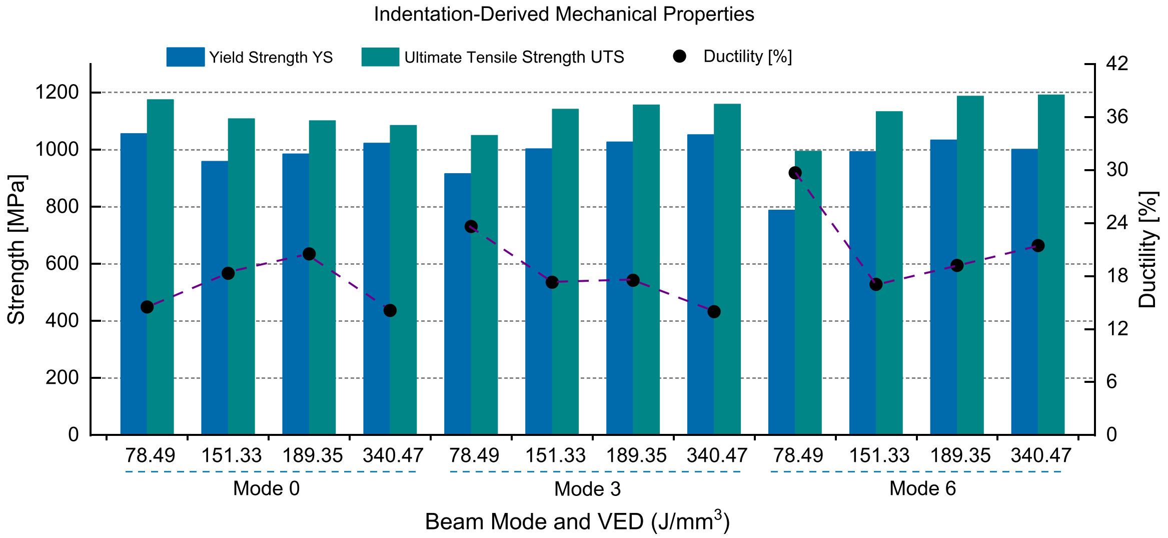

Fig. 20. Indicative yield strength (YS), ultimate tensile strength (UTS), and ductility index (D) derived from instrumented indentation measurements for different beam profiles and VED conditions.

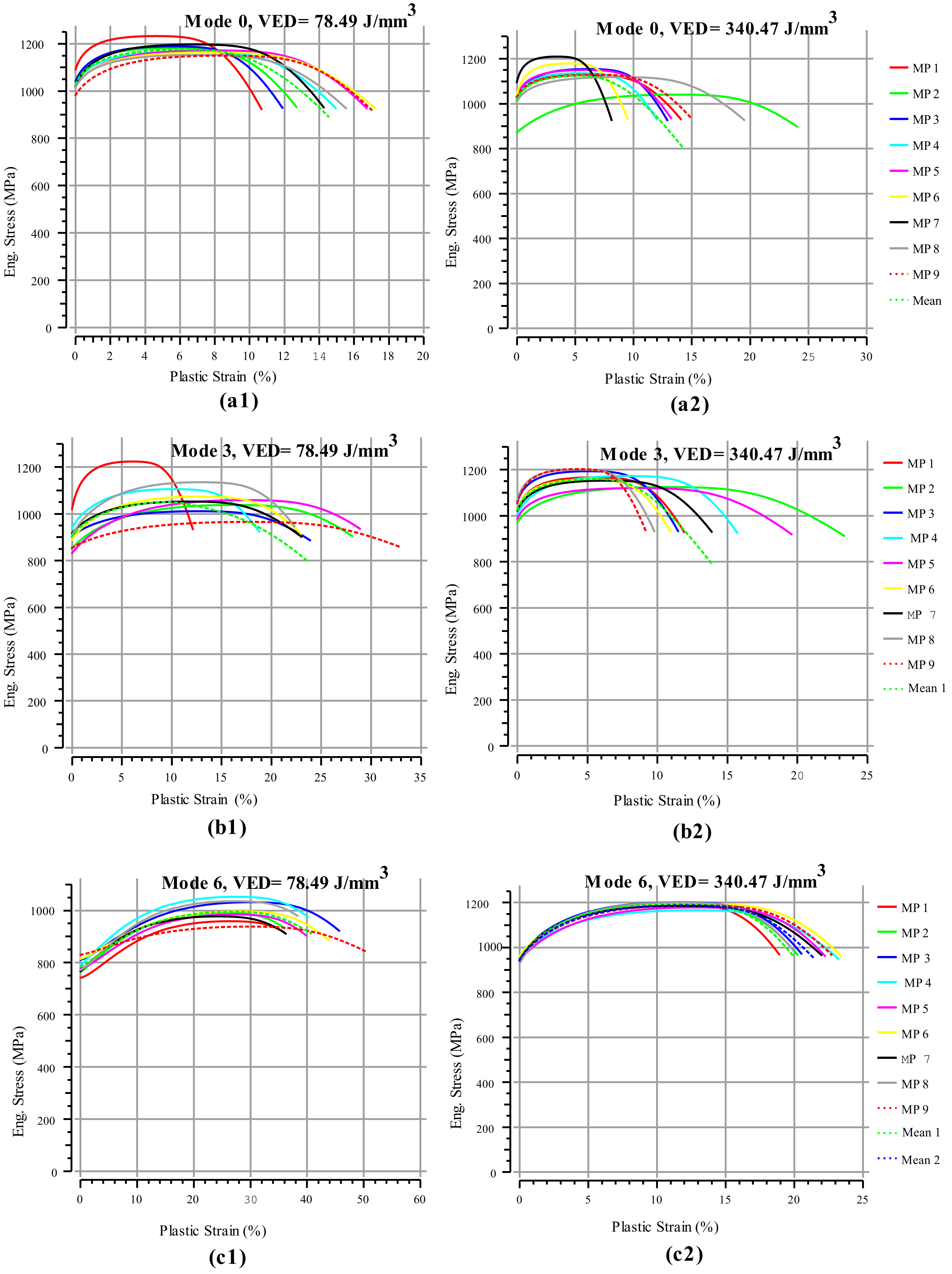

Fig. 21. Representative instrumented indentation-derived stress–strain curves for beam profiles Mode 0 (a1–a2), Mode 3 (b1–b2), and Mode 6 (c1–c2) at low (78.49 J/mm³) and high (340.47 J/mm³) VED conditions, illustrating the influence of beam shaping and energy input on the mechanical response of as-built Ti-6Al-4V.

cause a decline in ductility at high VED levels as indicated by the indentation-based tests. When the energy input is normalized using the measured track dimensions (Fig. 22), the shaped beams exhibit comparable effective energy conditions to the Gaussian case, indicating that their improved performance arises from a more uniform and efficient energy redistribution rather than simply higher nominal energy input. Mode 3 benefits from improved melt pool stability and more uniform energy distribution, producing smoother surfaces, reduced porosity, and continuous prior-β grain growth with well-aligned α′ laths. These structural refinements drive steady increases in UTS and YS with rising VED. However, ductility decreases even as relative density improves from < 98 % to ∼99.5 %. This apparent contradiction indicates that, beyond a certain densification threshold, porosity becomes a secondary factor in mechanical performance. Instead, microstructural effects, such as strong grain alignment, martensitic hardening, and residual stress accumulation dominate, limiting plastic strain accommodation and leading to reduced ductility despite the near-full density. This behavior is consistent with prior findings that porosity strongly governs strength and ductility in the high-porosity regime but that microstructural state and residual stresses control deformation behavior once relative density exceeds ∼99 % [74,75]. In similar findings, Vrancken et al. [76] also reported that ductility is primarily controlled by microstructural state rather than porosity, with post-processing heat treatments that transform α′ into α+ β lamellae significantly improving elongation. Mode 6 demonstrates the most balanced process–structure–property relationship. Its broader, shallower melt pool geometry promotes stable thermal gradients, smoother surfaces, and minimal porosity throughout the VED range. This stability yields a refined microstructure with continuous, well-aligned β-grains and uniform α′ lath growth. Consequently, Mode 6 achieves both high indicative strength (UTS up to ∼1192 MPa) and stable ductility (∼19–21 %), reflecting an optimal combination of defect suppression, uniform microstructure, and reduced stress localization. The mechanical performance achieved with the ring-shaped beam was comparable to the Gaussian case, consistent with previous findings that reported negligible loss in strength (≤ 2.5 % difference in UTS) and slightly improved ductility when using ring-beam profiles [77]. This suggests that beam shaping can enhance process stability and surface quality without compromising mechanical integrity, as also reported in the recent study [78]. The relatively stable ductility of the ring-based profiles results from their fine and homogeneous α′ morphology combined with minimal porosity, which together promotes strain accommodation and delays crack initiation compared to the coarser and more heterogeneous structure observed in Mode 0 [57,79]. Overall, these findings confirm that surface roughness and porosity, governed by melt pool stability, dictate the quality of the microstructure, which in turn drives the mechanical response. Modes 3 and 6 broaden the processing window, enabling smoother surfaces, near-full densification, and stable grain morphologies, which collectively translate into predictable and superior strength–ductility combinations. In contrast, Mode 0 is more prone to instability at elevated energy levels, where surface irregularities, increased porosity, and disrupted microstructures collectively degrade mechanical performance.

6. Future outlook

This study covers several fundamental aspects and provides insights into how different beam shapes and laser energy input affect surface quality, porosity, microstructural characteristics, and mechanical properties in PBF-LB/M of Ti-6Al-4V. However, research on laser beam shaping remains at an early stage, requiring deeper investigation into both process fundamentals and practical implementation. Thermal accumulation effects were not directly monitored in this study, therefore, future studies could integrate in-situ diagnostics, such as infrared or multispectral imaging, to capture melt pool dynamics and substrate preheating. Complementary simulation approaches, including space partitioning with dynamic mesh adaptation [80] or multi-scale enthalpy-based thermal modeling [81], may further improve predictive capabilities.

Future work should also expand to more complex builds and geometries, with systematic variations in hatch spacing, layer thickness, and scan strategies. Such efforts would enable the development of process maps for ring beam profiles and support reproducibility across different machines. Further studies should evaluate the trade-off between energy input and process robustness to determine the overall energy efficiency of ring-based profiles. In addition, investigating the maximum stable melt-pool size achievable with alternative beam shapes will help define their productivity limits and practical operating windows. The approach could be extended to lattice structures to assess how spatial energy distribution affects manufacturability and performance. Standard tensile testing is further required to fully establish the process–structure–property relationship. Additional research into residual stress characterization, using X-ray diffraction (XRD), neutron diffraction, or contour methods, could help explain the reduced ductility observed in dense ring-beam specimens and guide stress-relief strategies. Real-time adaptive control of beam profiles may offer further optimization opportunities for complex geometries or critical sections. Exploring new beam configurations, such as ring profiles with C:R ratios of 30:70 or 20:80, together with modified volumetric energy density calculations that consider actual beam diameters, could also support process refinement. In this study, the term “wider processing window” refers to the relatively broader range of stable processing conditions observed under the tested nominal VED settings. However, since identical nominal VEDs do not correspond to equivalent local energy inputs across different beam shapes, ongoing work will focus on normalizing the effective energy density and beam-intensity distributions to enable a direct comparison of processing windows among various beam profiles. Additionally, future work should also consider the practical trade-offs of beam shaping, including system complexity and implementation cost, to assess its scalability for industrial adoption. Ultimately, establishing robust correlations between beam shape, microstructure evolution (grain morphology and phase content), and mechanical properties will be essential for qualifying parts in high-performance applications [82,83]. Beyond the scope of this study, the outcomes provide a foundation for optimizing laser beam shaping strategies applicable to a wide range of materials and machine platforms. Future research in collaboration with industry will be essential to translate these findings into scalable solutions for high-throughput, defect-controlled PBF-LB/M production.

7. Conclusion

This study provides a comprehensive analysis of how laser beam shaping and energy input influence surface quality, porosity, microstructure, and mechanical behavior in PBF-LB/M of Ti-6Al-4V. By experimentally correlating these characteristics with tailored spatial energy distributions, the work advances understanding of how laser energy controls process stability, thermal behavior, and solidification characteristics, as reflected in the resulting microstructural and mechanical responses. The findings show that adjusting beam profiles and energy input can significantly enhance manufacturability and provide practical guidance for optimizing process parameters to achieve consistent quality and reliability. The key conclusions are summarized below:

1. Beam-shape-dependent heat distribution strongly influences melt-pool stability and surface morphology. The transition from the Gaussian beam (Mode 0) to ring-based energy profiles (Modes 3 and 6) reduces peak intensity, stabilizes melt flow, and suppresses spatter and recoil-pressure fluctuations, producing smoother surfaces and more uniform surface texture even at relatively high energy levels.
2. Defect formation and densification behavior depend on how energy is spatially distributed within the beam. Mode 0 produces nearly full density at relatively low nominal energy input (∼99.8 %) but

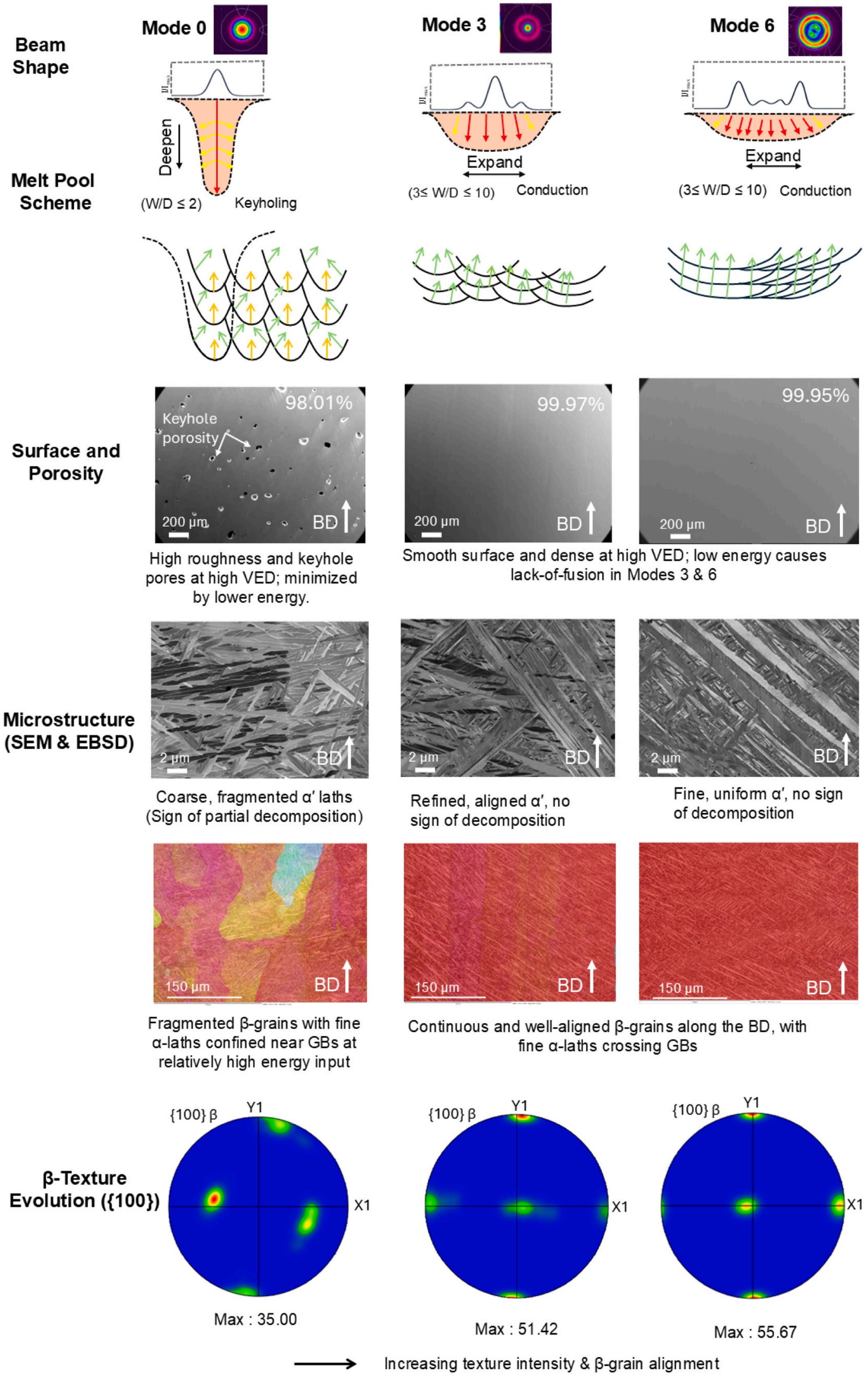

Fig. 22. Schematic–experimental summary showing how beam shape and energy input influence melt pool behavior, surface quality, microstructure, and β-texture evolution in PBF-LB/M Ti-6Al-4V.

transitions to keyhole porosity and reduced density ($\sim$96.8 %) at higher values due to localized overheating and unstable melt flow. In contrast, Modes 3 and 6 redistribute energy laterally, delaying the transition to keyholing, maintaining conduction-mode melting, and achieving near-full densification ($\sim$99.9 %) at higher effective energy levels (as confirmed by normalized areal energy-density analysis). This balance between lack-of-fusion and keyhole regimes demonstrates that beam shaping effectively stabilizes melting behavior and broadens the practical processing window.

3. Microstructural evolution is closely linked to beam-induced melt-pool geometry. Mode 6, characterized by a broader and shallower melt pool, promotes continuous columnar β-grain growth and stronger $\langle 001 \rangle$ alignment, while the narrower, deeper pools formed with Mode 0 favor grain fragmentation and local misorientation.
4. Although α'-martensite remains the dominant phase across all conditions, shaped beams promote more homogeneous lath alignment across grain boundaries, indicating steadier solidification and reduced local overheating compared to Mode 0.
5. The local mechanical response is driven more by microstructural uniformity than by density alone. Shaped beams, particularly Mode 6, achieve high indicative strength and stable ductility by minimizing stress-concentrating defects, promoting uniform α'-martensite morphology, and ensuring consistent load transfer across the microstructure.
6. Beam shaping offers a pathway toward scalable and reliable AM. By redistributing laser energy rather than merely increasing power, it enables stable melting at higher scan speeds while preserving part integrity. The relationships between spatial energy distribution, melt-pool stability, and defect formation revealed in this work provide a transferable foundation for optimizing laser–material interaction across different alloys and PBF-LB/M systems.

Overall, this work establishes a physical basis for laser beam shaping to expand the stable processing window, suppress defect formation, and tailor microstructure and properties in PBF-LB/M. These findings hold direct relevance for both academic research and industrial development of next-generation additive manufacturing strategies. While laser beam shaping demonstrates clear potential to enhance process stability and part quality, its practical implementation may involve trade-offs such as increased optical system complexity, alignment sensitivity, and cost, which should be carefully considered in future industrial applications.

CRediT authorship contribution statement

Dirk Herzog: Writing – review & editing, Writing – original draft, Visualization, Supervision, Resources, Funding acquisition. **Alexander E. Medvedev:** Writing – review & editing, Writing – original draft, Visualization, Validation, Software. **Abid Ullah:** Writing – review & editing, Writing – original draft, Visualization, Validation, Software, Investigation, Formal analysis, Data curation, Conceptualization. **Milan Brandt:** Writing – review & editing, Visualization, Validation, Supervision, Resources, Funding acquisition, Formal analysis. **Ingomar Kelbassa:** Writing – review & editing, Supervision, Project administration, Funding acquisition. **Tingting Liu:** Writing – review & editing, Visualization, Supervision, Software. **Andrey Molotnikov:** Writing – review & editing, Writing – original draft, Validation, Supervision, Resources.

Declaration of Competing Interest

The authors declare that they have no known competing financial interests or personal relationships that could have appeared to influence the work reported in this paper.

Acknowledgments

This project has received funding from the European Union's Horizon 2020 research and innovation program under the Marie Skłodowska-Curie grant agreement No 101034328. This paper reflects only the author's view, and the Research Executive Agency and the European Commission are not responsible for any use that may be made of the information it contains.

Appendix A. Supporting information

Supplementary data associated with this article can be found in the online version at doi:10.1016/j.jmatprotec.2026.119197.

Data availability

Data will be made available on request.

References

[1] Narasimharaju, S.R., Zeng, W., See, T.L., Zhu, Z., Scott, P., Jiang, X., Lou, S., 2022. A comprehensive review on laser powder bed fusion of steels: processing, microstructure, defects and control methods, mechanical properties, current challenges and future trends. J. Manuf. Process 75, 375–414. https://doi.org/10.1016/j.jmapro.2021.12.033.

[2] McConnell, S., Tanner, D., Kourousis, K.I., 2024. Productivity improvement opportunities for metal powder bed fusion technologies: a systematic literature review. Rapid Prototyp. J. 30, 231–246. https://doi.org/10.1108/RPJ-09-2023-0333.

[3] Schmidt, M., Cvecek, K., Duflou, J., Vollertsen, F., Arnold, C.B., Matthews, M.J., 2024. Dynamic beam shaping—Improving laser materials processing via feature synchronous energy coupling. CIRP Ann. 73, 533–559. https://doi.org/10.1016/j.cirp.2024.05.005.

[4] Stoll, T., Prudlik, R., Birg, M., Wudy, K., 2024. Influence of different beam shapes on melt pool geometry of single melt tracks on IN718. Prog. Addit. Manuf. https://doi.org/10.1007/s40964-024-00775-x.

[5] Nabavi, S.F., Farshidianfar, A., Dalir, H., 2023. A comprehensive review on recent laser beam welding process: geometrical, metallurgical, and mechanical characteristic modeling. Int. J. Adv. Manuf. Technol. 129, 4781–4828. https://doi.org/10.1007/s00170-023-12536-1.

[6] Suder, W., Chen, X., Sierra, D.R., Chen, G., Wainwright, J., Rajamudili, K., Pardal, G.R., Williams, S., 2024. Control of meltpool shape in laser welding. Weld. World 68, 1485–1495. https://doi.org/10.1007/s40194-024-01719-3.

[7] Paillier, G., Prätzsch, N., 2024. Beam shaping to tackle laser powder bed fusion challenges. PhotonicsViews 21, 30–35. https://doi.org/10.1002/phvs.202400021.

[8] Bakhtari, A.R., Sezer, H.K., Canyurt, O.E., Eren, O., Shah, M., Marimuthu, S., 2024. A review on laser beam shaping application in laser-powder bed fusion. Adv. Eng. Mater. 26, 2302013. https://doi.org/10.1002/adem.202302013.

[9] Tumkur, T.U., Voisin, T., Shi, R., Depond, P.J., Roehling, T.T., Wu, S., Crumb, M.F., Roehling, J.D., Guss, G., Khairallah, S.A., Matthews, M.J., 2024. Nondiffractive beam shaping for enhanced optothermal control in metal additive manufacturing. Sci. Adv. 7, eabg9358. https://doi.org/10.1126/sciadv.abg9358.

[10] Brezinski, M.E.: 5 - OPTICAL COHERENCE TOMOGRAPHY THEORY. In: Brezinski, M.E. (ed.) Optical Coherence Tomography. pp. 97–145. Academic Press, Burlington (2006).

[11] Yin, J., Wang, D., Yang, L., Wei, H., Dong, P., Ke, L., Wang, G., Zhu, H., Zeng, X., 2020. Correlation between forming quality and spatter dynamics in laser powder bed fusion. Addit. Manuf. 31, 100958. https://doi.org/10.1016/j.addma.2019.100958.

[12] Ur Rehman, A., Mahmood, M.A., Ansari, P., Pitir, F., Salamci, M.U., Popescu, A.C., Mihailescu, I.N., 2021. Spatter formation and splashing induced defects in laser-based powder bed fusion of alsi10mg alloy: a novel hydrodynamics modelling with empirical testing. Metals 11. https://doi.org/10.3390/met11122023.

[13] Yang, X., Li, Y., Li, B., 2023. Formation mechanisms of lack of fusion and keyhole-induced pore defects in laser powder bed fusion process: a numerical study. Int. J. Therm. Sci. 188, 108221. https://doi.org/10.1016/j.ijthermalsci.2023.108221.

[14] Bayat, M., Thanki, A., Mohanty, S., Witvrouw, A., Yang, S., Thorborg, J., Tiedje, N. S., Hattel, J.H., 2019. Keyhole-induced porosities in Laser-based Powder Bed Fusion (L-PBF) of Ti6Al4V: high-fidelity modelling and experimental validation. Addit. Manuf. 30, 100835. https://doi.org/10.1016/j.addma.2019.100835.

[15] Buffa, G., Costa, A., Palmeri, D., Pollara, G., Fratini, L., 2024. Defining a new process window for LPBF of Ti-6Al-4V based on micro-warping phenomena. CIRP J. Manuf. Sci. Technol. 52, 1–11. https://doi.org/10.1016/j.cirpj.2024.05.012.

[16] Ullah, A., Ur Rehman, A., Salamci, M.U., Pıtır, F., Liu, T., 2022. The influence of laser power and scanning speed on the microstructure and surface morphology of Cu2O parts in SLM. Rapid Prototyp. J. 28, 1796–1807. https://doi.org/10.1108/RPJ-12-2021-0342.

[17] Wischeropp, T., 2021. Adv. Sel. Laser Melting Laser Beam Shap. https://doi.org/10.1007/978-3-662-64585-7.

[18] Grigoriev, S.N., Gusarov, A.V., Metel, A.S., Tarasova, T.V., Volosova, M.A., Okunkova, A.A., Gusev, A.S., 2022. Beam shaping in laser powder bed fusion: péclet number and dynamic simulation. Metals 12. https://doi.org/10.3390/met12050722.

[19] Kliner, D., Kingsbury, A., 2024. The shape of things to come. PhotonicsViews 21, 59–63. https://doi.org/10.1002/phvs.202400012.

[20] Lei, J., Xie, J., Zhou, S., Song, H., Song, X., Zhou, X., 2019. Comparative study on microstructure and corrosion performance of 316 stainless steel prepared by laser melting deposition with ring-shaped beam and Gaussian beam. Opt. Laser Technol. 111, 271–283. https://doi.org/10.1016/j.optlastec.2018.09.057.

[21] Ayoola, W.A., Suder, W.J., Williams, S.W., 2019. Effect of beam shape and spatial energy distribution on weld bead geometry in conduction welding. Opt. Laser Technol. 117, 280–287. https://doi.org/10.1016/j.optlastec.2019.04.025.

[22] Holla, V., Kopp, P., Grünewald, J., Wudy, K., Kollmannsberger, S., 2023. Laser beam shape optimization in powder bed fusion of metals. Addit. Manuf. 72, 103609. https://doi.org/10.1016/j.addma.2023.10360.

[23] Singh, J., Oliveira, J.P., Taylor, H., Mireles, J., Wicker, R., 2024. A holistic approach for evaluation of Gaussian versus ring beam processing on structure and properties in laser powder bed fusion. J. Mater. Process Technol. 325, 118293. https://doi.org/10.1016/j.jmatprotec.2024.118293.

[24] Wischeropp, T.M., 2021. Effect of Laser Beam Profile on SLM Process. Advancement of Selective Laser Melting by Laser Beam Shaping. Springer Berlin Heidelberg, Berlin, Heidelberg, pp. 61–112.

[25] Bauch, A., Kohlwes, P., Kelbassa, I., 2025. Surface roughness formation in powder bed fusion of copper using gaussian and ring-shaped laser beam profiles. Lasers Manuf. Mater. Process. https://doi.org/10.1007/s40516-025-00313-9.

[26] King, W.E., Barth, H.D., Castillo, V.M., Gallegos, G.F., Gibbs, J.W., Hahn, D.E., Kamath, C., Rubenchik, A.M., 2014. Observation of keyhole-mode laser melting in laser powder-bed fusion additive manufacturing. J. Mater. Process Technol. 214, 2915–2925. https://doi.org/10.1016/j.jmatprotec.2014.06.00.

[27] Baskin, N., Yuce, C.: Effect of process parameters on the mechanical behavior of Ti6Al4V alloys fabricated by laser powder bed fusion method. Journal of Materials Research and Technology. 30, https://doi.org/10.1016/j.jmrt.2024.05.0843.

[28] Richter, J., Wegener, T., Kratzsch, R., Vollmer, M., Peuker, U., Niendorf, T., 2023. On the structural integrity and fatigue performance of additively manufactured Ti-6Al-4V parts processed using mechanically recycled powders. Int. J. Fatigue 176, 107903. https://doi.org/10.1016/j.ijfatigue.2023.107903.

[29] Plessis, Adu, Yadroitsava, I., Yadroitsev, I., 2020. Effects of defects on mechanical properties in metal additive manufacturing: a review focusing on X-ray tomography insights. Mater. Des. 187, 108385. https://doi.org/10.1016/j.matdes.2019.108385.

[30] Ullah, A., Bakhtari, A.R., Medvedev, A.E., Molotnikov, A., Herzog, D., Kelbassa, I., Emmelmann, C., Brandt, M., 2025. Effects of laser beam shaping on Ti-6Al-4V single tracks in PBF-LB/M: a study with Aconity MIDI+. Opt. Laser Technol. 192, 113762. https://doi.org/10.1016/j.optlastec.2025.113762.

[31] Plessis, Adu, Sperling, P., Beerlink, A., Tshabalala, L., Hoosain, S., Mathe, N., le Roux, S.G., 2018. Standard method for microCT-based additive manufacturing quality control 1: porosity analysis. MethodsX 5, 1102–1110. https://doi.org/10.1016/j.matdes.2019.108385.

[32] Clyne, T.W., Campbell, J.E., Burley, M., Dean, J., 2021. Profilometry-based inverse finite element method indentation plastometry (https://doi.org/https:/doi.org/). Adv. Eng. Mater. 23, 2100437. https://doi.org/10.1002/adem.202100437.

[33] Kim, J., Kim, K.-H., Kwon, D., 2016. Evaluation of high-temperature tensile properties of Ti-6Al-4V using instrumented indentation testing. Met. Mater. Int. 22, 209–215. https://doi.org/10.1007/s12540-016-5619-3.

[34] Metelkova, J., de Formanoir, C., Haitjema, H., Witvrouw, A., Pfleging, W., Hooreweder, B.: Elevated edges of metal parts produced by laser powder bed fusion: characterization and post-process correction. (2019).

[35] Metzbower, E.A., 1993. Keyhole formation. Metall. Trans. B 24, 875–880. https://doi.org/10.1007/BF02663148.

[36] Yang, J., Schlenger, L.M., Nasab, M.H., Van Petegem, S., Marone, F., Logé, R.E., Leinenbach, C., 2024. Experimental quantification of inward Marangoni convection and its impact on keyhole threshold in laser powder bed fusion of stainless steel. Addit. Manuf. 84, 104092. https://doi.org/10.1016/j.addma.2024.104092.

[37] Yang, T., Liu, T., Liao, W., Wei, H., Zhang, C., Chen, X., Zhang, K., 2021. Effect of processing parameters on overhanging surface roughness during laser powder bed fusion of AlSi10Mg. J. Manuf. Process 61, 440–453. https://doi.org/10.1016/j.addma.2024.104092.

[38] Snyder, J.C., Thole, K.A., 2020. Understanding laser powder bed fusion surface roughness. J. Manuf. Sci. Eng. 142. https://doi.org/10.1115/1.4046504.

[39] Bhatt, A., Huang, Y., Leung, C.L.A., Soundarapandiyan, G., Marussi, S., Shah, S., Atwood, R.C., Fitzpatrick, M.E., Tiwari, M.K., Lee, P.D., 2023. In situ characterisation of surface roughness and its amplification during multilayer single-track laser powder bed fusion additive manufacturing. Addit. Manuf. 77, 103809. https://doi.org/10.1016/j.addma.2023.103809.

[40] Patel, S., Rogalsky, A., Vlasea, M., 2020. Towards understanding side-skin surface characteristics in laser powder bed fusion. J. Mater. Res 35, 2055–2064. https://doi.org/10.1557/jmr.2020.125.

[41] Wei, M., Ding, W.J., Vastola, G., Zhang, Y.-W., 2022. Quantitative study on the dynamics of melt pool and keyhole and their controlling factors in metal laser melting. Addit. Manuf. 54, 102779. https://doi.org/10.1016/j.addma.2022.102779.

[42] Bauch, A., Kohlwes, P., Kelbassa, I., 2025. Surface roughness formation in powder bed fusion of copper using gaussian and ring-shaped laser beam profiles. Lasers Manuf. Mater. Process. https://doi.org/10.1007/s40516-025-00313-9.

[43] Kohlwes, P.: Light Engineering für die Praxis Prozessstabile additive Fertigung durch spritzerreduziertes Laserstrahlschmelzen Herausgegeben von Claus Emmelmann. (2024).

[44] Schwarzkopf, K., Burger, S., Chechik, L., Forster, C., Döring, M., Spurk, C., Hummel, M., Olowinsky, A., Beckmann, F., Moosmann, J., Schmidt, M., 2024. Revealing the influence of ring-shaped beam profiles in high-speed laser beam microwelding by synchrotron x-ray imaging. J. Laser Appl. 36, 042027. https://doi.org/10.2351/7.0001582.

[45] Luo, X., Yang, W., Li, Y., 2024. The influence of laser beam shaping on surface roughness, surface figure and mid-spatial frequency of fused silica glass in CO2 laser smoothing. Opt. Laser Technol. 171, 110426. https://doi.org/10.1016/j.optlastec.2023.110426.

[46] Jost, E.W., Miers, J.C., Robbins, A., Moore, D.G., Saldana, C., 2021. Effects of spatial energy distribution-induced porosity on mechanical properties of laser powder bed fusion 316L stainless steel. Addit. Manuf. 39, 101875. https://doi.org/10.1016/j.addma.2021.101875.

[47] Kan, W.H., Gao, M., Zhang, X., Liang, E., Chiu, N.S.L., Lim, C.V.S., Huang, A., 2022. The influence of porosity on Ti-6Al-4V parts fabricated by laser powder bed fusion in the pursuit of process efficiency. Int. J. Adv. Manuf. Technol. 119, 5417–5438. https://doi.org/10.1007/s00170-021-08374-8.

[48] Martin, A.A., Calta, N.P., Khairallah, S.A., Wang, J., Depond, P.J., Fong, A.Y., Thampy, V., Guss, G.M., Kiss, A.M., Stone, K.H., Tassone, C.J., Nelson Weker, J., Toney, M.F., van Buuren, T., Matthews, M.J., 2019. Dynamics of pore formation during laser powder bed fusion additive manufacturing. Nat. Commun. 10, 1987. https://doi.org/10.1038/s41467-019-10009-2.

[49] Chaudry, M.A., Mohr, G., Hilgenberg, K., 2022. Experimental and numerical comparison of heat accumulation during laser powder bed fusion of 316L stainless steel. Prog. Addit. Manuf. 7, 1071–1083. https://doi.org/10.1007/s40964-022-00282-x.

[50] Huang, Y., Fleming, T.G., Clark, S.J., Marussi, S., Fezzaa, K., Thiyagalingam, J., Leung, C.L.A., Lee, P.D., 2022. Keyhole fluctuation and pore formation mechanisms during laser powder bed fusion additive manufacturing. Nat. Commun. 13, 1170. https://doi.org/10.1038/s41467-022-28694-x.

[51] Tan, C.Y., Wen, C., Mayes, E., Zhang, D., Ang, H.Q., 2025. Revealing the limits of laser energy density: a study of the combined effects of process parameters on melt pool and microstructure in WE43 magnesium alloys (https://doi.org/https:/doi.org/). J. Magnes. Alloy. 13, 1034–1049. https://doi.org/10.1016/j.jma.2025.01.019.

[52] Wang, K., Xie, D., Lv, F., Liu, F., Liu, R., Liu, D., Zhao, J., 2023. Stability of molten pool and microstructure evolution of Ti-6Al-4 V during laser powder bed fusion with a flat-top beam. Addit. Manuf. 75, 103756. https://doi.org/10.1016/j.addma.2023.103756.

[53] Chechik, L., Schwarzkopf, K., Rothfelder, R., Grünewald, J., Schmidt, M., 2024. Material dependent influence of ring/spot beam profiles in laser powder bed fusion. Addit. Manuf. Lett. 9, 100211. https://doi.org/10.3390/met11121989.

[54] Grünewald, J., Gehringer, F., Schmöller, M., Wudy, K., 2021. Influence of Ring-Shaped Beam Profiles on Process Stability and Productivity in Laser-Based Powder Bed Fusion of AISI 316L. Met. (Basel) 11. https://doi.org/10.3390/met11121989.

[55] Qian, C., Zhang, K., Zhu, J., Liu, Y., Liu, Y., Liu, J., Liu, J., Yang, Y., Wang, H., 2024. Effect of processing parameters on the defects, microstructure, and property evaluation of Ti-6Al-4V titanium alloy processed by laser powder bed fusion. AIP Adv. 14, 025246. https://doi.org/10.1063/7.0001251.

[56] Xu, J., Zhu, J., Fan, J., Zhou, Q., Peng, Y., Guo, S., 2019. Microstructure and mechanical properties of Ti–6Al–4V alloy fabricated using electron beam freeform fabrication. Vacuum 167, 364–373. https://doi.org/10.1016/j.vacuum.2019.06.030.

[57] Vilaro, T., Colin, C., Bartout, J.D., 2011. As-fabricated and heat-treated microstructures of the Ti-6Al-4V alloy processed by selective laser melting. Metall. Mater. Trans. A 42, 3190–3199. https://doi.org/10.1007/s11661-011-0731-y.

[58] Mayer, T., Friso, F., Radis, R., 2025. Effect of build orientation on thermal expansion of LPBF printed Ti-6Al-4V. Metall. Mater. Trans. A 56, 1287–1309. https://doi.org/10.1007/s11661-025-07706-7.

[59] Zarei, M. amin, Shabestari, M.G., Shabestari, S.G., Abedi, H., 2025. Microstructural heterogeneity and anisotropic mechanical properties of titanium alloys manufactured by wire arc additive manufacturing: a review. J. Mater. Res. Technol. 36, 8381–8409. https://doi.org/10.1016/j.jmrt.2025.05.106.

[60] Dilip, J.J.S., Zhang, S., Teng, C., Zeng, K., Robinson, C., Pal, D., Stucker, B., 2017. Influence of processing parameters on the evolution of melt pool, porosity, and microstructures in Ti-6Al-4V alloy parts fabricated by selective laser melting. Prog. Addit. Manuf. 2, 157–167. https://doi.org/10.1007/s40964-017-0030-2.

[61] Shipley, H., McDonnell, D., Culleton, M., Coull, R., Lupoi, R., O'Donnell, G., Trimble, D., 2018. Optimisation of process parameters to address fundamental challenges during selective laser melting of Ti-6Al-4V: a review. Int. J. Mach. Tools Manuf. 128, 1–20. https://doi.org/10.1016/j.ijmachtools.2018.01.003.

[62] Byres, N.E., da Fonseca, J.Q., Daniel, C.S., Donoghue, J., Davis, A.E., Shanthraj, P., Dod, B., Prangnell, P.B., 2021. The evolution of abnormally coarse grain structures in beta-annealed Ti-6Al%-4V% rolled plates, observed by in-situ investigation. Acta Mater. 221, 117362. https://doi.org/10.1016/j.actamat.2021.117362.

[63] Ren, Y.M., Lin, X., Yang, H.O., Tan, H., Chen, J., Jian, Z.Y., Li, J.Q., Huang, W.D., 2021. Microstructural features of Ti-6Al-4V manufactured via high power laser directed energy deposition under low-cycle fatigue. J. Mater. Sci. Technol. 83, 18–33. https://doi.org/10.1016/j.jmst.2020.12.026.

[64] Medvedev, A.E., Brudler, S., Piegert, S., Illston, T., Qian, M., Brandt, M., 2025. Interlayer time as a robust, geometry-agnostic predictor of microstructural and mechanical properties evolution in PBF-LB/M Ti6Al4V alloy. J. Mater. Process Technol. 340, 118858. https://doi.org/10.1016/j.jmatprotec.2025.118858.

[65] Brudler, S., Medvedev, A.E., Pandelidi, C., Piegert, S., Illston, T., Qian, M., Brandt, M., 2024. Systematic investigation of performance and productivity in

laser powder bed fusion of Ti6Al4V up to 300 μm layer thickness. J. Mater. Process Technol. 330, 118450. https://doi.org/10.1016/j.jmatprotec.2024.118450.

[66] Qiu, C., Ravi, G.A., Dance, C., Ranson, A., Dilworth, S., Attallah, M.M., 2015. Fabrication of large Ti–6Al–4V structures by direct laser deposition. J. Alloy. Compd. 629, 351–361. https://doi.org/10.1016/j.jallcom.2014.12.234.

[67] Zhang, G., Lu, X., Li, J., Chen, J., Lin, X., Wang, M., Tan, H., Huang, W., 2022. In-situ grain structure control in directed energy deposition of Ti6Al4V. Addit. Manuf. 55, 102865. https://doi.org/10.1016/j.addma.2022.102865.

[68] Wainwright, J., Williams, S., Ding, J., 2023. Refinement of Ti-6Al-4V prior-β grain structure in the as-deposited condition via process control during wire-direct energy deposition. Addit. Manuf. 74, 103712. https://doi.org/10.1016/j.addma.2023.103712.

[69] Xian, G., Oh, J. mok, Lee, J., Cho, S.M., Yeom, J.-T., Choi, Y., Kang, N., 2022. Effect of heat input on microstructure and mechanical property of wire-arc additive manufactured Ti-6Al-4V alloy. Weld. World 66, 847–861. https://doi.org/10.1007/s40194-021-01248-3.

[70] Praveen Kumar, D., Vinoth Jebaraj, A., 2022. Role of volumetric energy density and post-heat treatments to achieve stable microstructure on additive manufactured Ti6Al4V alloy. Trans. Indian Inst. Met. 75, 3077–3085. https://doi.org/10.1007/s12666-022-02688-1.

[71] Zhao, R., Chen, C., Wang, W., Cao, T., Shuai, S., Xu, S., Hu, T., Liao, H., Wang, J., Ren, Z., 2022. On the role of volumetric energy density in the microstructure and mechanical properties of laser powder bed fusion Ti-6Al-4V alloy. Addit. Manuf. 51, 102605. https://doi.org/10.1016/j.addma.2022.102605.

[72] Lu, S.L., Zhang, Z.J., Liu, R., Qu, Z., Wang, B., Zhou, X.H., Eckert, J., Zhang, Z.F., 2022. Prior β grain evolution and phase transformation of selective laser melted Ti6Al4V alloy during heat treatment. J. Alloy. Compd. 914, 165235. https://doi.org/10.1016/j.jallcom.2022.165235.

[73] Neikter, M., Huang, A., Wu, X., 2019. Microstructural characterization of binary microstructure pattern in selective laser-melted Ti-6Al-4V. Int. J. Adv. Manuf. Technol. 104, 1381–1391. https://doi.org/10.1007/s00170-019-04002-8.

[74] Völker, B., Maier-Kiener, V., Werbach, K., Müller, T., Pilz, S., Calin, M., Eckert, J., Hohenwarter, A., 2019. Influence of annealing on microstructure and mechanical properties of ultrafine-grained Ti45Nb. Mater. Des. 179, 107864. https://doi.org/10.1016/j.matdes.2019.107864.

[75] Pathania, A., Subramaniyan, A.K., Nagesha, B.K., 2022. Influence of post-heat treatments on microstructural and mechanical properties of LPBF-processed Ti6Al4V alloy. Prog. Addit. Manuf. 7, 1323–1343. https://doi.org/10.1007/s40964-022-00306-6.

[76] Vrancken, B., Thijs, L., Kruth, J.-P., Van Humbeeck, J., 2012. Heat treatment of Ti6Al4V produced by Selective Laser Melting: Microstructure and mechanical properties. J. Alloy. Compd. 541, 177–185. https://doi.org/10.1016/j.jallcom.2012.07.022.

[77] Cozzolino, E., Tiley, A.J., Ramirez, A.J., Astarita, A., Herderick, E.D., 2024. Energy efficiency of Gaussian and ring profiles for LPBF of nickel alloy 718. Int. J. Adv. Manuf. Technol. 132, 3093–3104. https://doi.org/10.1007/s00170-024-13511-0.

[78] Wu, B., Gao, H., Huang, Y., Li, S., Chen, Z., Li, W., Chen, H., Wei, Q., 2025. Comparative study of dot-ring and Gaussian beams on epitaxial grain growth and crack suppression of DD6 superalloy fabricated by laser powder bed fusion. Mater. Sci. Eng. A 947, 149181. https://doi.org/10.1016/j.msea.2025.149181.

[79] Qiu, C., Aswathanarayanaswamy, R., Dance, C., Ranson, A., Dilworth, S., Attallah, M., 2015. Fabrication of large Ti–6Al–4V structures by direct laser deposition. J. Alloy. Compd. 629, 351–361. https://doi.org/10.1016/j.jallcom.2014.12.234.

[80] Foteinopoulos, P., Papacharalampopoulos, A., Stavropoulos, P., 2024. Additive manufacturing simulations: An approach based on space partitioning and dynamic 3D mesh adaptation. Addit. Manuf. Lett. 11, 100256. https://doi.org/10.1016/j.msea.2025.149181.

[81] Stavropoulos, P., Pastras, G., Souflas, T., Tzimanis, K., Bikas, H., 2022. A computationally efficient multi-scale thermal modelling approach for PBF-LB/M based on the enthalpy method. Metals 12. https://doi.org/10.3390/met12111853.

[82] Han, C., Zou, Y., Dong, Z., Hu, G., Xu, S., Yang, Y., Wang, D., 2025. Manipulating martensite transformation to achieve superior strength-ductility synergy in laser powder bed fusion of nickel-aluminium-bronze alloy via heat treatments. Virtual Phys. Prototyp. 20, e2478227. https://doi.org/10.1080/17452759.2025.2478227.

[83] Meng, F., Liogas, K.A., Lau, K.B., Deng, Y., Korsunsky, A.M., Wang, P., Shen, X., Lee, C.H.T., 2025. The selection of scanning strategy and annealing schedule for the optimization of texture and magnetic properties of Fe-3.5 wt%Si alloy parts fabricated by laser powder bed fusion. Addit. Manuf. 97, 104614. https://doi.org/10.1016/j.addma.2024.104614.